Ceramics International 51 (2025) 60217–60233

Contents lists available at ScienceDirect

Ceramics International

journal homepage: www.elsevier.com/locate/ceramint

Biogenic fabrication of S-scheme NiO–$FeWO_4$ heterojunction nanocomposite using Cassava *(Manihot esculenta Crantz)* leaf extract for visible-light-driven dye degradation: Synthesis, characterisation and photocatalytic evaluation

Fatimah Lee [a], Luqman Chuah Abdullah [b], Irmawati Ramli [a], Ahmad Adlie Shamsuri [c], Rusli Daik [d], Ikhwan Syafiq Mohd Noor [e], Siti Nurul Ain Md Jamil [a,e,*]

[a] Department of Chemistry, Faculty of Science, Universiti Putra Malaysia UPM, 43400, Serdang, Selangor, Malaysia
[b] Department of Chemical and Environmental Engineering, Faculty of Engineering, UPM, 43400, Serdang, Selangor, Malaysia
[c] Laboratory of Biocomposite Technology, Institute of Tropical Forestry and Forest Products, Universiti Putra Malaysia UPM, 43400, Serdang, Selangor, Malaysia
[d] Department of Chemical Sciences, Faculty of Science and Technology, Universiti Kebangsaan Malaysia UKM, 43600, Bangi, Selangor, Malaysia
[e] Centre for Foundation Studies in Science of Universiti Putra Malaysia UPM, 43400, Serdang, Selangor, Malaysia

ARTICLE INFO

Handling Editor: Dr P. Vincenzini

Keywords:
S-scheme
NiO-$FeWO_4$ heterojunction
Photodegradation
Visible-light

ABSTRACT

Industrial dye effluents such as methylene blue (MB) resist biodegradation, generate carcinogenic intermediates and bioaccumulate in ecosystems, demanding advanced remediation strategies. Photocatalysis utilizing semiconductor-based materials as photocatalysts offers a sustainable route. Nickel oxide (NiO), a p-type semiconductor, exhibits excellent hole mobility, however suffers from wide bandgap, limited to UV-light activity and rapid charge recombination. In this study, coupling NiO with a narrow bandgap n-type semiconductor, iron (II) tungstate ($FeWO_4$) has successfully extended its light absorption and enhances charge separation, improving the photocatalytic activity of NiOnps. An S-scheme NiO-$FeWO_4$ heterojunction nanocomposite was fabricated *via* PEG-200 binder-assisted physical coupling technique, using Cassava leaves extract (CMLE) as a natural reducing and stabilising agent. FTIR analysis confirms the coupling of NiOnps and $FeWO_4$nps through vibrational modes of Ni-O, Fe-O, W-O and O-WO bonds. XRD analysis shows an enhanced crystallinity of NiO-$FeWO_4$ heterojunction nanocomposite (88.73 %) compared to pristine NiOnps (75.14 %) and $FeWO_4$nps (66.54 %). FESEM and HRTEM images of NiO-$FeWO_4$ depict a clear interfacial contact of granular $FeWO_4$nps onto rod-like NiOnps, with narrow PDI values indicating the feasibility of CMLE to maintain size uniformity. The p-n heterojunction formation significantly reduced the bandgap energy from 2.82 eV to 2.10 eV, suppressed PL intensity, depleted charge transfer resistance and enhanced photocurrent response. Hence, NiO-*40*$FeWO_4$ nanocomposite demonstrates outstanding photocatalytic performance under visible light irradiation towards MB (10 ppm) degradation (96.72 %) with a rate constant of 0.04996 min^{-1}, far surpassing pristine NiOnps (21.90 %, 0.0035 min^{-1}) and FeW-O_4nps (60.45 %, 0.0023 min^{-1}). This work presents a synergistic strategy that integrates biogenic synthesis and capability of binder-assisted coupling technique to design heterojunction formation, yielding a robust photocatalyst with enhanced structural, electronic and optical properties for sustainable wastewater remediation.

1. Introduction

Industrial dye effluents remain a persistent threat to water security. Synthetic dyes used in textile processing are designed for chemical stability [1] and resist biodegradation [2] where they impair photosynthesis of microalgae [3], disrupt microbial balance and infiltrate human food chains [4]. Cationic methylene blue (MB) is a widely used thiazine dye that can form intermediate carcinogenic compounds and toxic aromatic amines, such as benzidine and 2-naphthylamine if not decomposed completely [4]. These intermediates persist in environment for years, bioaccumulate in tissues of aquatic organisms and contaminate human food chain, posing risks such as bladder cancer, dermatitis and

* Corresponding author. Department of Chemistry, Faculty of Science, Universiti Putra Malaysia UPM, 43400, Serdang, Selangor Darul Ehsan, Malaysia.
E-mail address: ctnurulain@upm.edu.my (S.N.A. Md Jamil).

https://doi.org/10.1016/j.ceramint.2025.10.220
Received 29 August 2025; Received in revised form 6 October 2025; Accepted 14 October 2025
Available online 16 October 2025
0272-8842/© 2025 Published by Elsevier Ltd.

pulmonary disorder [5]. Therefore, urgent development of effective water-treatment technologies is essential to mitigate the adverse effects of dye residues on the environment, human health and aquatic ecosystems.

Over the decades, several techniques have been developed to treat dye-contaminated water, such as biological treatment [6], adsorption [7], membrane filtration and advanced oxidation processes (AOPs) [8]. Amongst, AOPs are proven to be an effective way to eliminate dyes from water environment, which relies on in-situ generation of highly reactive oxygen species like hydroxyl (·OH) and superoxide radicals ($\cdot O_2^-$), to decompose complex organic compounds [9]. This includes ozonation, electrolysis, Fenton reaction and photocatalysis [10]. Photocatalysis stands out due to its ability to break down complex compounds, requiring only light irradiation to activate photocatalytic reaction, making the process more sustainable, cost-effective and pollution-free, without the use of toxic and hazardous chemical reagents [11].

Metal oxides semiconductor such as zinc oxide (ZnO) [12–15], tin (IV) oxide (SnO_2) [16–18], copper oxide (CuO) [19,20] and titanium dioxide (TiO_2) [21–23] have been extensively studied as photocatalysts for environmental remediation owing to their high photocatalytic efficiency [12,16,20,24]. However, their wide bandgap energies restrict the excitation of electrons to only ultraviolet (UV) light region (<400 nm) [25]. Moreover, single metal oxides typically suffer from rapid electron-hole recombination, which limits charge carrier availability for redox reactions essential for efficient photocatalysis [26]. Nickel oxide (NiO), a p-type semiconductor with a wide bandgap (~3.6 eV), also suffers from limited visible-light absorption and rapid electron-hole recombination. Nonetheless, NiO offers excellent chemical and thermal stability, strong oxidation capacity, non-toxic, low-cost, outstanding hole mobility and high theoretical specific capacitance, making it a valuable material in diverse applications, such as gas sensing [27], dye-sensitized solar cells and supercapacitors [28].

To tackle this problem and leverage the excellent properties of NiO, this study presents a synergistic approach to design a heterostructure photocatalyst, by coupling two semiconductors to enhance charge separation, reduce bandgap and extend light absorption into visible region, thereby requiring lower energy compared to UV-light to excite electrons. Formation of p-n heterojunction with n-type semiconductor has been an ideal solution in many research [28–32]. However, ensuring low charge recombination rate and efficient charge transfer without compromising strong redox potential as suggested in S-scheme pathway, requires careful selection of the n-type semiconductor. This considers factors including bandgap energy, band alignment and work function [33]. Given this requirement, tungstate-based materials, specifically iron (II) tungstate ($FeWO_4$) offer assuring compatibility with NiO. $FeWO_4$ possesses narrow bandgap (2.0–2.8 eV), well-matched conduction and valence band positions to NiO and lower work function (4.32 eV) than NiO (5.20 eV), enabling visible light absorption. $FeWO_4$ exhibits stable band structures and has great durability in extreme conditions for industrial applications [34].

Heterojunction nanocomposites can be fabricated by several approaches such as physical mixing and in-situ growth methods, each with distinct advantages and limitations. Conventional physical mixing of pre-synthesised semiconductors offers simplicity, low-cost, scalability and flexible composition control, but often suffers from poor interfacial contact, which hinder efficient charge transfer [35]. In contrast, in-situ growth methods *via* hydrothermal and co-precipitation, where one semiconductor is grown directly on the surface of another, provide a proper lattice orientation, resulting in intimate interfacial contact, thus more effective charge separation [36]. However, this method requires longer reaction time, higher energy consumption and specific conditions [35]. To address these trade-offs, this work explores a modified physical mixing strategy, called binder-assisted physical coupling method, where a polymer-based binder, polyethylene glycol 200 (PEG-200), was employed as a non-covalent bridging agent to promote interfacial contact between NiO and $FeWO_4$ nanoparticles. PEG-200, owing to its ether linkages and terminal hydroxyl groups, is commonly used as a structure-directing agent and chelating agents capable of binding through multiple coordinate interactions to form stable complexes [37–39]. Its low molecular weight (190–200 g/mol) facilitates better dispersion and faster adsorption onto nanoparticle surfaces [40].

Various methods have been explored to synthesise nanoparticles, such as hydrothermal [41], sol-gel [42] and chemical precipitation [11]. However, these methods often require reaction time of over 20 h [43–45] and long gelation and drying time, which induces gel shrinkage and cracking [25,46]. Chemical precipitation method is favoured due to its low operating cost, mild reaction conditions and ability to produce high yields of nanoparticles [47], however its reliance on chemical reagents (e.g., ascorbate, sodium borohydride, Tollen's reagent, ammonium hydroxide, surfactants) remain a notable challenge [47,48]. In contrast, biogenic route utilizing plant extracts as natural reducing and stabilising agent offers a facile, sustainable and non-toxic alternative. This green approach is biodegradable, reduces the need of high-energy equipment, can be performed under mild conditions and generates minimal to no hazardous wastes [49]. Several plant extracts have been studied for nanoparticles synthesis including *Sapindus mukorossi* [50], fruit peel waste (e.g., tangerine, banana) [51–53], *Averrhoa carambola* fruit [54], *Dimocarpus longan* fruit [55], *Stevia rebaudiana* leaves [56] and *Artemisia vulgaris* leaves [57]. However, their potential practical application in large-scale production are hindered by seasonal time constraint, region-specific availability and reproducibility issues arising from batch-to-batch variability, particularly in the case of fruit peel wastes [58].

In this context, the NiO and $FeWO_4$ nanoparticles were synthesised *via* a biogenic route employing Cassava *(Manihot esculenta Crantz)* leaves extract as the reducing and stabilising agent. Cassava plant is a woody shrub native to South America and now cultivated globally as a staple food crop. It grows well in marginal soils, with its starchy tubers harvested as a major carbohydrate source, while the leaves are discarded and treated as agricultural waste or used for animal feed [59–61], leaving a large surplus biomass suitable for valorisation. The Cassava leaves are rich in phytochemicals such as flavonoids, alkaloids, polyphenols, and phenolic acids [62], which contain abundant hydroxyl groups (-OH) and carboxylic acid groups (-COOH), to facilitate metal ion reduction [63]. A phytochemical profiling of Cassava leaves by GC-MS and HPLC revealed a high flavonoid content (35.19 %; isoginkgetin, retinal, scutellarein tetramethyl ether and isolongifolol), phenolic acids (30.06 %; gallic acid, ferulic acid, chlorogenic acid, caffeic acid, ellagic acid, coumaric acid and cinnamic acid) and moderate quantities (0.46–2.0 %) of tannins and saponins [62], highlighting its potential in sustainable nanoparticle synthesis. There are limited literatures reported on the use of Cassava leaves extract, despite its high phytochemical content.

Therefore, this study aimed to explore the feasibility of Cassava leaves extract (CMLE) as reducing and stabilising agent in the synthesis of NiOnps and $FeWO_4$nps and PEG-200 as binder in NiO-$FeWO_4$ heterojunction fabrication. The NiOnps, $FeWO_4$nps and PEG-200-assisted NiO-$FeWO_4$ heterojunction nanocomposites were characterised to elucidate their structural, optical, morphological and colloidal properties. Photocatalytic performance of NiO-$FeWO_4$ heterojunction nanocomposite as a novel photocatalysts was evaluated through photodegradation of MB under visible light irradiation. This sustainable synthesis strategy not only aims to enhance photocatalytic performance but also aligns with environmental and economic objectives: low-cost operation, energy saving, non-toxic conditions and support the United Nations Sustainable Development Goals - SDG 6 and SDG 12. Ultimately, this work contributes to the advancement of green nanotechnology for wastewater remediation.

2. Methodology

2.1. Chemicals and reagents

Cassava (*Manihot Esculenta Crantz)* leaves were purchased from local market in Serdang, Selangor, Malaysia. Nickel (II) nitrate ($Ni(NO_3)_2 \cdot 6H_2O$) (SYSTERM), iron (II) sulphate ($FeSO_4 \cdot 7H_2O$), sodium tungstate ($Na_2WO_4 \cdot 2H_2O$) and polyethylene glycol 200 (PEG-200) (R&M Chemicals, UK). Distilled water, methanol, n-hexane and ethanol were used as solvents. Methylene blue (R&M Chemicals, UK) was used as model dye pollutant to evaluate the photocatalytic activity of synthesised nanocomposite. Details on the materials are provided in the Supporting Information (Text S1).

2.2. Extraction of Cassava (Manihot esculenta Crantz) leaves

The extraction of Cassava leaves was carried out *via* maceration technique using methanol and n-hexane as the solvents. The fresh leaves were dried in the oven at 50 °C overnight after being thoroughly washed with distilled water. The dried leaves were ground into powder and macerated in methanol (1:10 w/v) for 3 days, with 20 min stirring each day. The mixture was filtered and the filtrate (crude extracts) was subjected to liquid-liquid extraction in n-hexane (1:1 v/v). Two layer of aqueous phase (methanol fraction) and organic phase (hexane fraction) were observed. The aqueous phase (bottom layer) was collected on glass Petri dish and concentrated using hot air oven at 50 °C. The obtained solid residue are labelled as CMLE, and kept at −4 °C to preserve the bioactive compounds. Prior to synthesis of nanoparticles, CMLE was dissolved in distilled water to obtain aqueous extract solution.

2.3. Synthesis of NiO nanoparticles

0.1 M of $Ni(NO_3)_2 \cdot 6H_2O$ solution was prepared in distilled water. An appropriate amount of CMLE was added dropwise into the solution under constant stirring of 270 rpm at 60 °C, for 3 h 0.1 M NaOH was added until pH 9 is achieved, to induce precipitation of $Ni(OH)_2$. The colloidal solution was then aged at room temperature (27.0 °C) overnight. The precipitate formed was filtered and dried at 120 °C for 5 h, then rinsed with ethanol/water (1:1 v/v) mixture several times and re-dried under the same condition. The powder obtained was calcined in tube furnace at 500 °C with heating rate of 5 °C/min for 3 h to obtain NiO nanoparticles (NiOnps).

2.4. Synthesis of $FeWO_4$ nanoparticles

0.1 M of $Na_2WO_4 \cdot 2H_2O$ and $FeSO_4 \cdot 7H_2O$ solutions were prepared separately in two beakers by dissolving the precursors in distilled water and sonicated for 10 min. The solutions were mixed and stirred at 270 rpm, followed by heating at 80 °C for 4 h. Concurrently, CMLE was added dropwise to the solution. The pH of the solution was adjusted to pH 11 using 0.1 M NaOH. The colloidal solution was aged overnight, followed by the filtration of the precipitate formed, oven-dried at 120 °C for 5 h, rinsed with ethanol/water mixture and re-dried. The powder obtained was calcined at 500 °C for 3 h, to obtain $FeWO_4$ nanoparticles ($FeWO_4$nps).

2.5. Fabrication of NiO-$FeWO_4$ heterojunction nanocomposite using PEG-200

NiO-$FeWO_4$ nanocomposites was prepared using the synthesised NiOnps and $FeWO_4$nps, with different weight fraction of $FeWO_4$nps (20 %, 30 %, 40 %, 50 % and 60 %). The NiOnps was dispersed in 50 mL ethanol and ultrasonicated for 10 min. PEG-200, at a mass ratio 1:2 (total mass: PEG-200) was added to the suspension, followed by $FeWO_4$nps and sonicated for another 10 min. The mixture was stirred at 200 rpm for 1 h at room temperature. The suspension was centrifuged (4000 rpm, 5 min), filtered and rinsed using ethanol/water (1:1 v/v) mixture several times. The product was dried at 80 °C overnight and annealed at 300 °C for 2 h. The photocatalysts were then labelled as NiO-*20*$FeWO_4$, NiO-*30*$FeWO_4$, NiO-*40*$FeWO_4$, NiO-*50*$FeWO_4$ and NiO-*60*$FeWO_4$, corresponds to $FeWO_4$nps content.

2.6. Characterisation

The synthesised NiOnps, $FeWO_4$nps and NiO-$FeWO_4$ nanocomposites were characterised through several techniques. The fourier-transform infrared spectroscopy (FTIR), X-ray diffraction (XRD), X-ray photoelectron spectroscopy (XPS), dynamic light scattering (DLS) analysis, zeta potential, field emission scanning electron microscopy (FESEM) with energy-dispersive X-ray (EDX) analysis, transmission electron microscopy (TEM), UV–Vis diffuse reflectance spectroscopy (DRS), photoluminescence (PL) spectroscopy, Brunauer-Emmett-Teller (BET) analysis and electron impedance spectroscopy (EIS), transient photocurrent response and Mott-Schottky (M − S) analysis. The fabrication procedure of working electrode using FTO glass substrate is explained in the Supporting Information (Text S2). The details on the conditions of the characterisation are provided in Text S3.

2.7. Adsorption equilibrium and photocatalytic experimental

The photocatalytic activity of NiOnps, $FeWO_4$nps and NiO-$FeWO_4$ nanocomposites were evaluated by dispersing 40 mg of the photocatalyst into 100 mL of 10 ppm methylene blue (MB) solution (pH = 7.11). Prior to that, adsorption equilibrium was established. The mixture was stirred at 120 rpm in the dark. Samples (3 mL) of the MB solution were collected at regular intervals until adsorption equilibrium was reached. As shown in Fig. 7(a), the adsorption equilibrium of MB reached after 60 min. Photocatalytic degradation was carried out under visible light irradiation ($\lambda \geq 420$ nm, 100 W LED lamp) at room temperature (25.0 °C). Upon irradiation, the mixture was stirred in the dark for 60 min to establish of adsorption equilibrium. During the photocatalytic reaction, a 3 mL aliquot of MB solution was withdrawn and filtered using 0.22 μ m Millipore syringe filter at regular time intervals until equilibrium was reached. The filtered aliquot was analysed using UV spectrophotometer (Dynamica HALODB) at λ = 663 nm. The photolysis of MB was also carried out. The adsorption and degradation efficiency of MB removal was calculated using Equation (1) [64]:

$$\text{Removal Efficiency } (\%) = \frac{C_o - C_t}{C_o} \times 100\% \quad (1)$$

where C_0 refers to the initial concentration of MB solution and C_t refers to the concentration of MB solution at any time interval.

3. Results and discussion

3.1. Structural properties: FTIR, XRD and XPS analysis

Fig. 1(a) displays the FTIR spectra of CMLE, NiOnps, $FeWO_4$nps, NiO-*20*$FeWO_4$, NiO-*30*$FeWO_4$, NiO-*40*$FeWO_4$, NiO-*50*$FeWO_4$ and NiO-*60*$FeWO_4$ nanocomposites. The enlarged spectrum of CMLE in Fig. 1(b) shows 6 absorption bands attributed to the presence of flavonoids, phenolic acids, tannins and saponins. Flavonoids are a group of compounds containing abundant -OH groups bonded to aromatic rings and cyclic ether (-C-O-C), while phenolic acids contain -COOH groups. The presence of these bioactive compounds were indicated by sharp absorption band at 1629 cm^{-1} representing –C=C and –CH of aromatic ring, -C-O of cyclic ether at 1048 cm^{-1}, -CH_2 of cyclohexane ring at 962 cm^{-1}, -OH stretching and bending vibrations at 3314 cm^{-1} and 1351 cm^{-1}, and 656 cm^{-1} absorption band representing –CH bending of aromatic rings. The absorption band at 2101 cm^{-1} was ascribed to -C ≡ N of linamarin compound in CMLE.

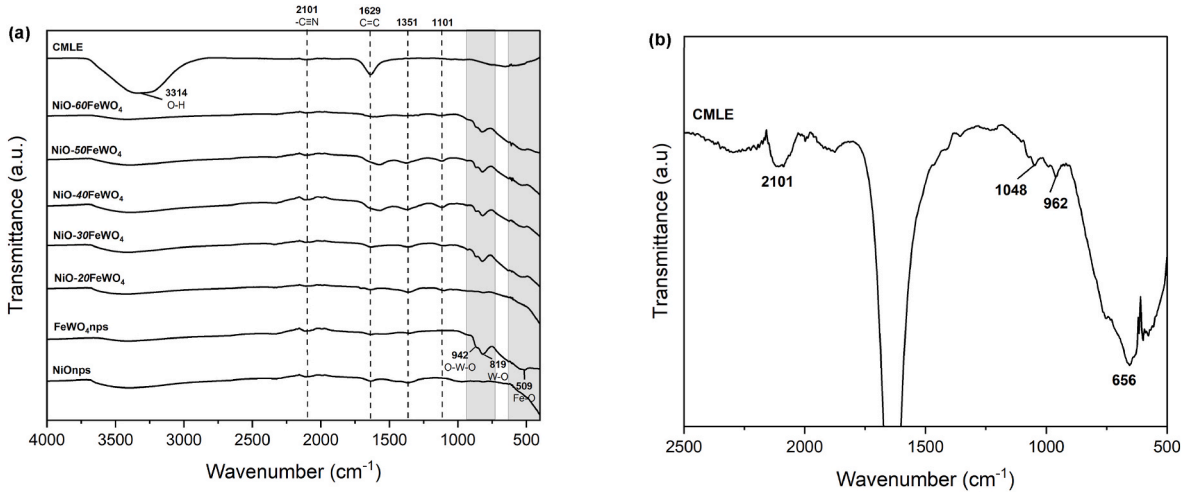

Fig. 1. (a) FTIR spectra of CMLE, NiOnps, $FeWO_4$nps, NiO-*20*$FeWO_4$, NiO-*30*$FeWO_4$, NiO-*40*$FeWO_4$, NiO-*50*$FeWO_4$ and NiO-*60*$FeWO_4$ nanocomposites and **(b)** enlarged FTIR spectrum of CMLE in the 2500–500 cm region.

As shown in the spectrum of NiOnps, the absorption band at around 590 cm^{-1} to 400 cm^{-1} was attributed to Ni-O bond. For $FeWO_4$nps, the absorption bands at 942 cm^{-1}, 819 cm^{-1} and 509 cm^{-1} were assigned to the stretching vibrations of O-W-O, W-O and Fe-O, respectively. The spectra of all NiO-$FeWO_4$ nanocomposites have similar appearance of absorption bands as NiO and $FeWO_4$, indicating the presence of Ni-O, O-W-O, W-O and Fe-O bonds. However, the absorption of Fe-O, W-O and Fe-O were not significantly observed in NiO-*20*$FeWO_4$ spectrum, which might be due to low content of $FeWO_4$ (20 wt%). The stretching vibration at 2101 cm^{-1} and 1629 cm^{-1} were still detected, indicating the presence of CMLE residue left on NiOnps, $FeWO_4$nps and NiO-$FeWO_4$ post-calcination. The appearance of absorption band at 1101 cm^{-1} for all NiO-$FeWO_4$ nanocomposites might be attributed to C-O-C stretching vibration of PEG-200 residue [65].

The crystalline phase structures of NiOnps, $FeWO_4$nps NiO-*20*$FeWO_4$, NiO-*30*$FeWO_4$, NiO-*40*$FeWO_4$, NiO-*50*$FeWO_4$ and NiO-*60*$FeWO_4$ nanocomposites were evaluated by XRD analysis. Fig. 2(a) shows the diffraction peaks of NiOnps at 37.05°, 43.15°, 62.87°, 75.56° and 79.41° were well-matched to JCPDS No. 47–1049, which determined a cubic crystalline structure (FCC) and a space group of Fm-3m. These peaks were indexed to the miller indices of (1 1 1), (2 0 0), (2 2 0), (3 1 1) and (2 2 2) crystal planes, respectively. The diffraction peaks of $FeWO_4$nps is well-matched with JCPDS No. 71–2390. The observed peaks at 23.70°, 30.36°, 36.23°, 41,24°, 53.57°, 61.45° and 64.70°, representing the plane of (0 1 1), (1 1 1), (0 2 1), (1 2 1), (2 0 2), (1 1 3) and (1 3 2), respectively. This pattern is well indexed into monoclinic wolframite of $FeWO_4$ and a space group of P2/c. These findings are consistent with those reported in the literatures [25,66,67]. In Fig. 2(b), the diffraction patterns of all NiO-$FeWO_4$ nanocomposites show combined characteristic peaks of both NiO and $FeWO_4$, indicating a

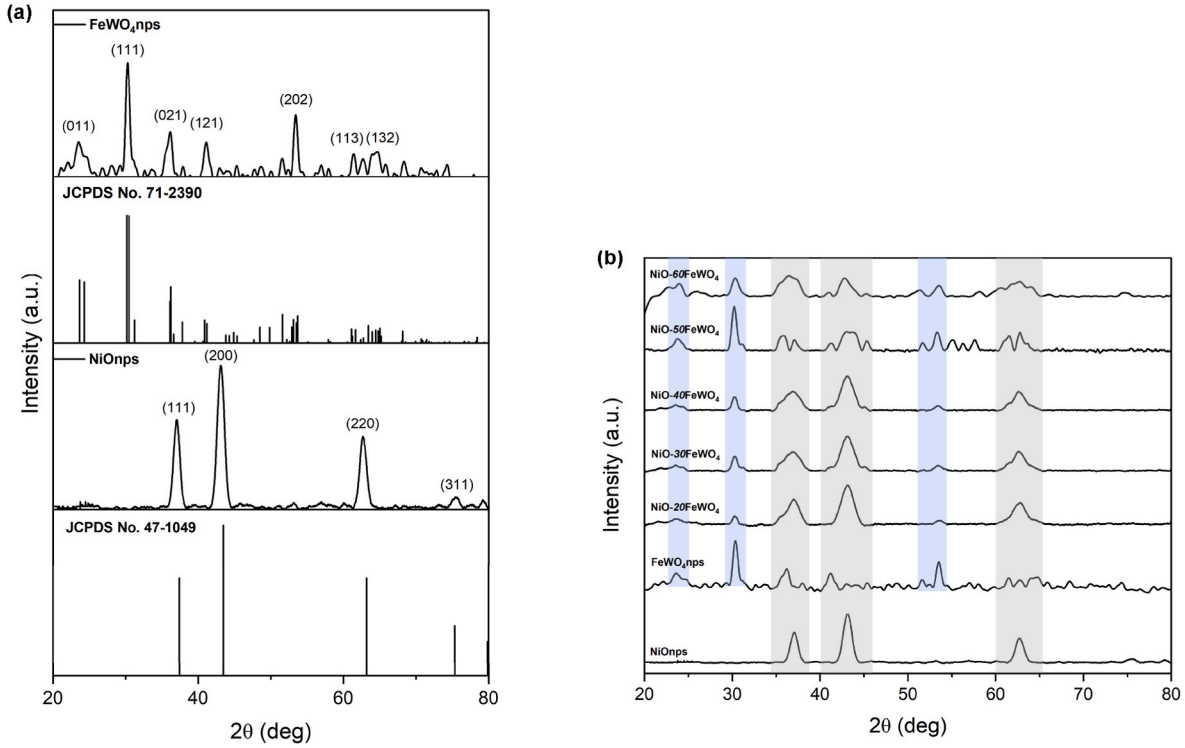

Fig. 2. (a) XRD patterns and standard patterns of NiOnps and $FeWO_4$nps and **(b)** XRD patterns of NiOnps, $FeWO_4$nps and all NiO-$FeWO_4$ nanocomposites.

successful coupling of NiOnps with $FeWO_4$nps.

The crystallite size, crystallinity and microstrain of NiOnps, $FeWO_4$nps, NiO-$FeWO_4$ nanocomposites were calculated using Equations (2)–(4) [68,69], respectively:

$$Debye-Scherer\ equation: \text{Crystallite size, D (nm)} = \frac{K\lambda}{\beta \cdot \cos\theta} \quad (2)$$

$$\text{Crystallinity (\%)} = \frac{\text{Area of crystalline peaks}}{\text{Area of total peaks}} \times 100\% \quad (3)$$

$$\text{Micro}-\text{strain}, \epsilon = \frac{\beta}{4 \cdot \tan\theta} \quad (4)$$

where K is Debye-Scherer constant (0.9), λ is the wavelength of CuK_α radiation, β is the FWHM (radians) of XRD peak at the diffraction angle and θ is the peak position (radians). Table 1 presents the average crystallite size, crystallinity and micro-strain of NiOnps, $FeWO_4$nps and all NiO-$FeWO_4$ nanocomposites. NiOnps has the smallest crystallite size (6.82 nm), while $FeWO_4$nps has the largest crystallite size (8.83 nm), which suggests that $FeWO_4$ crystallise in larger domains. The crystallite sizes of NiO-$FeWO_4$ decreases slightly as $FeWO_4$ content increases. The sharp and intense diffraction peaks of NiOnps indicate good crystallinity (75.0 %) and more well-ordered atomic planes while $FeWO_4$nps with low-intensity peaks usually ascribed to amorphous region [63], shows lower crystallinity (66.54 %), which possibly has more defects in the lattice planes [70]. Interestingly, NiO-*20*$FeWO_4$, NiO-*30*$FeWO_4$ and NiO-*40*$FeWO_4$ nanocomposites exhibit better crystallinity than pristine NiOnps and $FeWO_4$nps. This indicates that the formation of heterojunction *via* PEG-200-assisted coupling technique promotes a more ordered atomic arrangement and reduces internal stress. However, the crystallinity drops for NiO-*50*$FeWO_4$ and NiO-*60*$FeWO_4$ nanocomposites, which could be due to excessive $FeWO_4$ loading that introduces more amorphous phase, resulting in defect-induced recombination. Micro-strain is closely related to lattice distortion from defects and internal stress [71]. NiOnps has the lowest micro-strain (1.10×10^{-2}) suggesting a low-defect lattice, while $FeWO_4$nps has slightly higher micro-strain (1.65×10^{-2}) which is due to its more complex structure. The NiO-*20*$FeWO_4$, NiO-*30*$FeWO_4$ and NiO-*40*$FeWO_4$ nanocomposites have similar micro-strain as $FeWO_4$. This shows that heterojunction formation not only improved the atomic order but also preserved lattice stability, without introducing additional lattice stress into the crystal. However, NiO-*50*$FeWO_4$ and NiO-*60*$FeWO_4$ shows significant increase, which could be due to mismatch of interplanar planes when $FeWO_4$nps dominates and agglomerates around NiOnps, consequently explains their low crystallinity.

The XPS analysis was carried out to determine the elemental composition and oxidation states of the elements present in the samples. As elucidated in Fig. 3(a), the XPS survey spectrum of NiOnps, $FeWO_4$nps and NiO-*40*$FeWO_4$ nanocomposite confirm the presence of Ni, Fe, W and O elements in pristine NiOnps and $FeWO_4$nps, and the co-existence of the elements in NiO-*40*$FeWO_4$ nanocomposite. Interfacial charge transfer can be indicated by the shifting of binding energies, where reduction in binding energy reflects increased electron density around the atom, and vice versa [72]. Fig. 3(b) displays the Ni 2p spectra of NiOnps and NiO-*40*$FeWO_4$ nanocomposite, where pristine NiOnps shows peaks at 879.38 eV and 871.73 eV correspond to Ni $2p_{1/2}$ (Ni^{2+}), and peaks at 853.63 eV and 855.85 eV, correspond to Ni $2p_{3/2}$ of Ni^{2+} and Ni^{3+} [72], respectively. The peak at 861.01 eV (Ni^{2+}) is the satellite peak. For NiO-*40*$FeWO_4$ nanocomposite, reduction by 0.23–0.74 eV of the peaks to lower binding energies were observed, suggesting interfacial charge transfer from n-type $FeWO_4$nps to p-type NiOnps, leading to an increase in electron density around Ni [73]. The O 1s spectra (Fig. 3 (c)) shows peaks at 529.10, 530.31 and 529.31 eV for NiOnps, $FeWO_4$nps and NiO-*40*$FeWO_4$, respectively, assigned to lattice oxygen (metal-oxygen bond) [74]. Pristine $FeWO_4$nps exhibits broader peaks and at slightly higher binding energy, due to mixed Fe-O and W-O bonds dominating the $FeWO_4$nps system. Furthermore, the peaks observed at 530.88 eV (NiOnps) and 530.76 eV (NiO-*40*$FeWO_4$) were associated to oxygen vacancies [75]. However, pristine $FeWO_4$nps does not show a distinct peak at similar binding energy due to its stoichiometrically stable wolframite structure and accommodates charge mainly *via* Fe^{2+}/Fe^{3+} redox flexibility rather than oxygen loss. Hence, coupling NiOnps with $FeWO_4$nps induces interfacial charge redistribution and introduces new oxygen vacancy states that is more pronounce in NiO-*40*$FeWO_4$. The peak at 532.28 eV (NiO-*40*$FeWO_4$) corresponds to surface adsorbed hydroxyl groups [76]. From Fig. 3(d), the Fe 2p spectrum of $FeWO_4$nps exhibits peaks at 723.80 eV (Fe $2p_{1/2}$, Fe^{2+}), 710.93 eV (Fe $2p_{3/2}$, Fe^{2+}) [77], 726.27 eV, (Fe $2p_{1/2}$, Fe^{3+}) and a satellite peak at 714.74 eV (Fe^{2+}) [78]. In NiO-*40*$FeWO_4$, these peaks were shifted to higher binding energy, consistent with electrons redistribution and Fermi level realignment at the heterojunction interface [79] as Fe loses electron density to NiOnps. Fig. 3(d) presents the W 4f spectrum with binding energy peaks of $FeWO_4$nps at 37.89 eV and 35.75 eV represent W $4f_{5/2}$ and W $4f_{7/2}$, relative to W^{6+}. NiO-*40*$FeWO_4$ also exhibits peaks at similar binding energies (37.87 eV (W $4f_{5/2}$) and 35.74 eV (W $4f_{7/2}$)), indicating a stable oxidation of W^{6+} upon heterojunction formation.

Table 1
Crystallite size, crystallinity and micro-strain of NiOnps, $FeWO_4$nps and NiO-$FeWO_4$ nanocomposites.

Sample	Average Crystallite Size (nm)	Crystallinity (%)	Micro-strain, ϵ
NiOnps	6.82	75.14	1.10×10^{-2}
$FeWO_4$nps	8.83	66.54	1.65×10^{-2}
NiO-*20*$FeWO_4$	7.18	88.03	1.63×10^{-2}
NiO-*30*$FeWO_4$	7.07	80.36	1.66×10^{-2}
NiO-*40*$FeWO_4$	6.94	77.26	1.65×10^{-2}
NiO-*50*$FeWO_4$	5.23	59.91	2.68×10^{-2}
NiO-*60*$FeWO_4$	7.42	54.89	2.06×10^{-2}

3.2. Optical and electrochemical properties: UV–vis DRS, photoluminescence (PL), EIS analysis and transient photocurrent response

The UV–Vis absorption spectra in Fig. 4(a) reveal that NiO-$FeWO_4$ nanocomposites show broad visible-light absorption, as $FeWO_4$nps loading increases, signifying that the heterojunction formation effectively extends the light-harvesting capability of NiOnps, rendering it photoactive within the visible light region. As expected, NiOnps exhibit strong absorption only in UV-light region, while $FeWO_4$nps shows broad absorption across the visible light region. Evidently, two absorption peaks (around 315 nm and 525 nm) were observed, which was assigned to NiOnps and $FeWO_4$nps, respectively. The estimated optical bandgap energy of NiOnps, $FeWO_4$nps and all NiO-$FeWO_4$ nanocomposites were calculated using the following Kubelka-Munk equation (5) [80]:

$$\alpha h\nu = A\left(h\nu - E_g\right)^{\frac{n}{2}} \quad (5)$$

where α refers to the absorption coefficient, h is Planck's constant, ν is the light frequency, A is a constant, E_g is the bandgap energy and n refers to the electronic transition (n = 1 for direct and n = 4 for indirect bandgap). The E_g value was obtained by extrapolating the linear region of $(\alpha h\nu)^{\frac{n}{2}}$ against $h\nu$ to $(\alpha h\nu)^{\frac{n}{2}} = 0$. Fig. 4(b) and (c) shows the Tauc plots of NiOnps, $FeWO_4$nps and NiO-$FeWO_4$ nanocomposites, whereas their respective bandgap values are tabulated in Table 2. The bandgap energy of NiOnps and $FeWO_4$nps were 2.82 eV and 2.04 eV, respectively. The bandgap of NiOnps was narrower than values commonly reported in

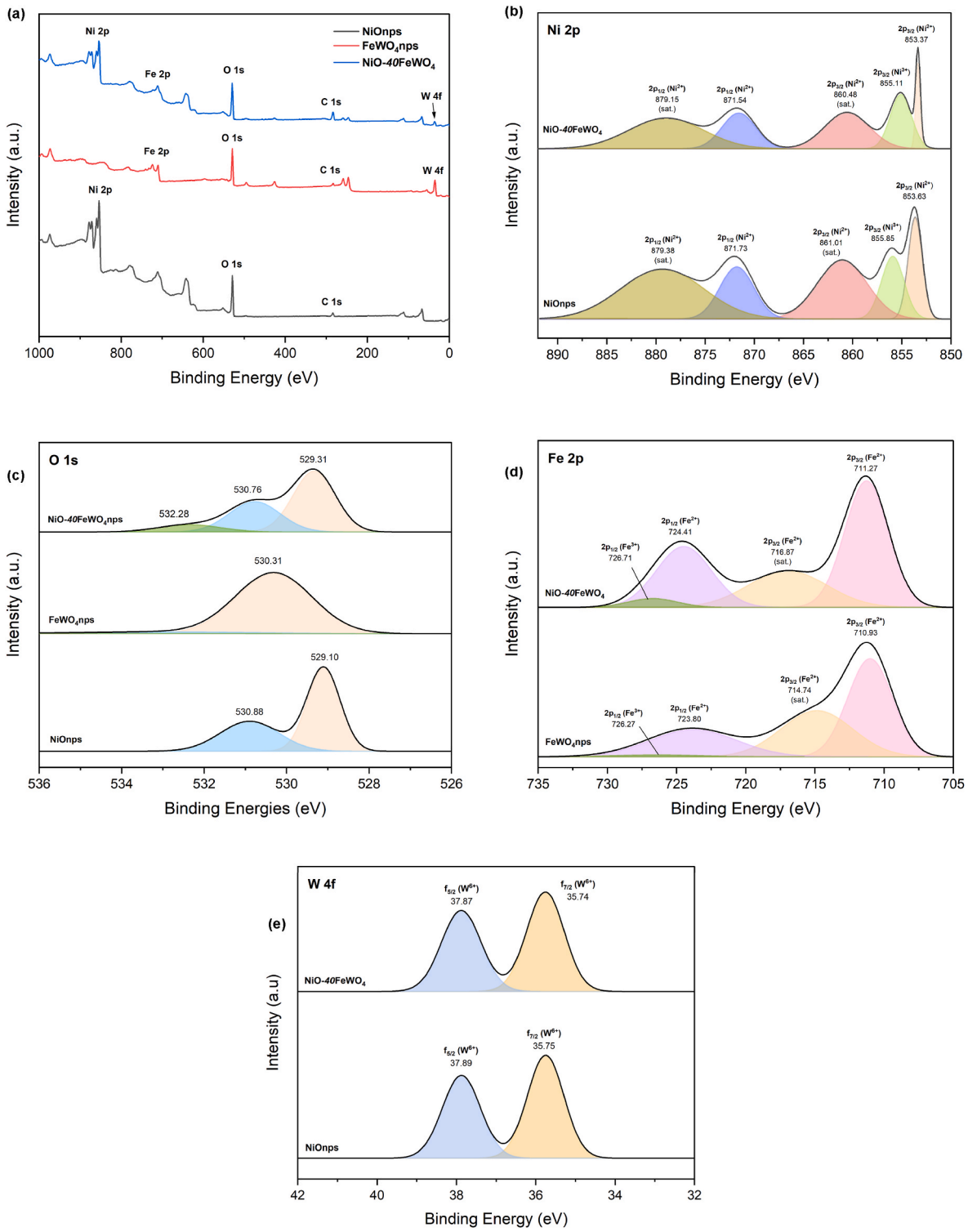

Fig. 3. **(a)** XPS survey spectra and high-resolution XPS spectra of **(b)** Ni 2p, **(c)** O 1s, **(d)** Fe 2p and **(e)** W 4f.

literatures, which were ~3.0–3.6 eV [81–84]. This can be attributed to the plant-mediated synthesis using CMLE, which often leaves residual organics on the surface of nanoparticles, introducing mid-gap defect states, resulting in reduction of the apparent bandgaps. This finding is consistent with several reported literatures, involving known wide bandgap metal oxides such as $SrTiO_3$, TiO_2 and NiO [83,85,86]. The bandgap energy of NiO-$FeWO_4$ nanocomposites decreases with increasing $FeWO_4$ content up until NiO-*40*$FeWO_4$ and a slight increase was observed for NiO-*50*$FeWO_4$ and NiO-*60*$FeWO_4$. This trend indicates that the heterojunction formation has successfully reduced the bandgap of NiOnps, from 2.82 eV to 2.10 eV, with 40 wt% of $FeWO_4$nps may be the optimal loading for an effective band-edge realignment between NiOnps and $FeWO_4$nps [87]. This also signifies that NiO-*40*$FeWO_4$ nanocomposite requires the lowest energy to excite electrons from valence band to conduction band compared to NiOnps alone, requiring the highest energy.

PL characterisation was employed to investigate the charge carrier recombination rate of NiOnps, $FeWO_4$nps and NiO-$FeWO_4$

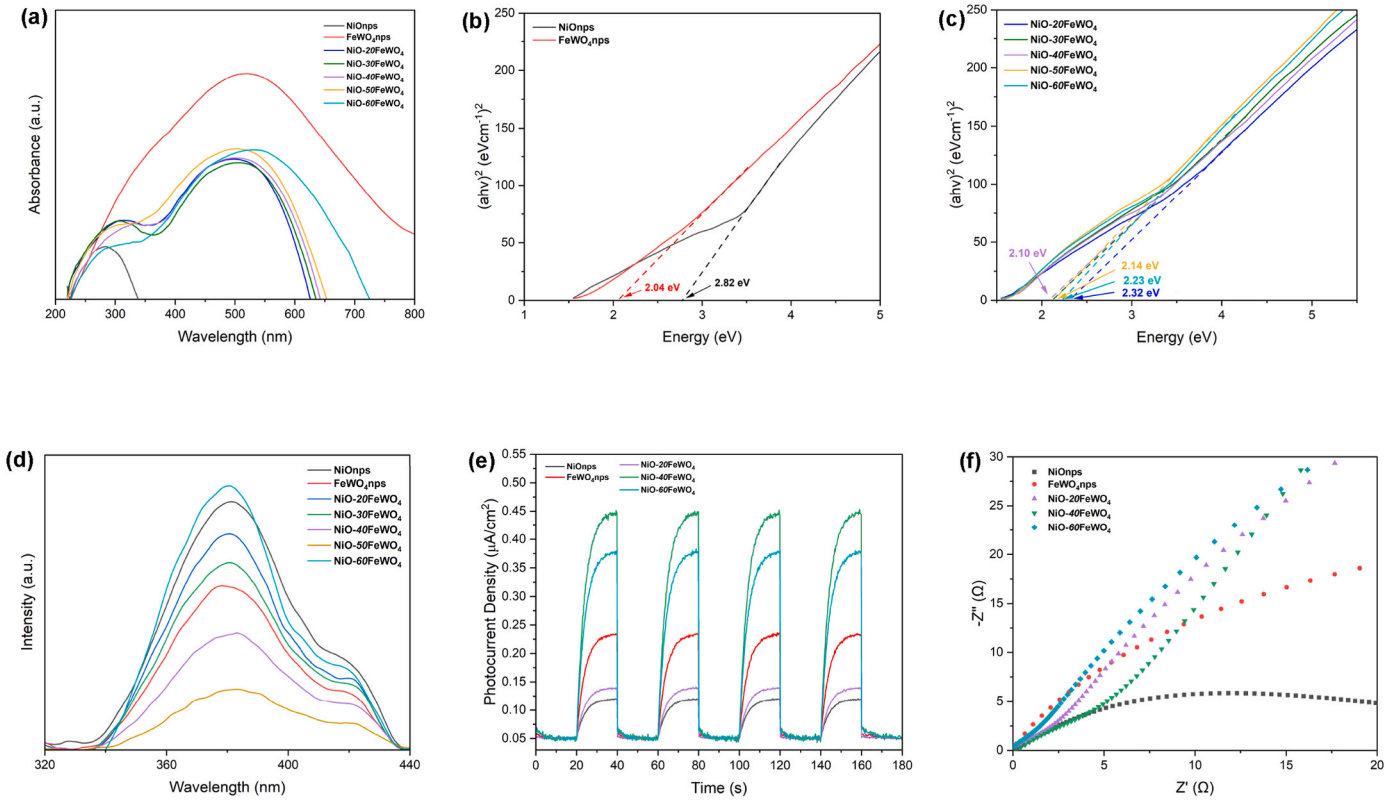

Fig. 4. **(a)** UV–vis diffuse reflectance spectra, **(b)–(c)** Tauc plots, **(d)** photoluminescence (PL) spectra, **(e)** photocurrent responses and **(f)** EIS Nyquist plot of NiOnps, $FeWO_4$nps and NiO-$FeWO_4$ nanocomposite.

Table 2
Bandgap energies of NiOnps, $FeWO_4$nps and NiO-$FeWO_4$ nanocomposites.

Samples	Bandgap, E_g (eV)
NiOnps	2.82
$FeWO_4$nps	2.04
NiO-*20*$FeWO_4$	2.32
NiO-*30*$FeWO_4$	2.14
NiO-*40*$FeWO_4$	2.10
NiO-*50*$FeWO_4$	2.14
NiO-*60*$FeWO_4$	2.23

nanocomposites. As shown in Fig. 4(d), the excitation wavelengths were observed at 380 and 421 nm. The PL emission spectra of NiO-$FeWO_4$ nanocomposites shows that the incorporation of $FeWO_4$nps onto the surface of NiOnps has significantly suppressed the intensity of NiOnps emission, as the content of $FeWO_4$nps increases. The reduced PL intensity was attributed to lower recombination rate of photogenerated charge carriers due to the synergistic formation of p-n heterojunction. However, NiO-*60*$FeWO_4$ shows higher PL intensity than NiOnps. This unusual observation might be caused by interfacial defects. This may happen when $FeWO_4$nps, with higher intrinsic oxygen defects dominate the system, thus charge carriers recombine more radiatively instead of being separated, leading to charge trapping and higher PL emission [88]. Similar trend was reported in the construction of Ag_3PO_4/NiO heterostructure composites, where the author explained that the enhancement was attributed to NiO acting as a charge carrier donor, thus electrons and holes settle within Ag_3PO_4, increasing the probability to recombine radiatively (Type I straddling gap) [88]. While NiO-*40*-$FeWO_4$ and NiO-*50*$FeWO_4$ exhibit lower PL intensity than $FeWO_4$nps, suggesting the optimal composition of $FeWO_4$nps.

Transient photocurrent responses (I-t) were conducted to further evaluate the charge carrier recombination rate. As depicted in Fig. 4(e), the I-t curves of four on/off cycles reveal that NiOnps exhibits the weakest photocurrent response, attributed to its high electron-hole recombination rate [89]. Pristine $FeWO_4$nps shows a stronger response, owing to its narrower bandgap and lower charge carrier recombination rate. Notably, the NiO-$FeWO_4$ nanocomposites demonstrate an enhanced photocurrent response, with NiO-*40*$FeWO_4$ exhibiting the highest response. This indicates that the heterojunction formation significantly promotes charge carrier separation and migration efficiency [90].

Electron impedance spectroscopy (EIS) was employed to evaluate the interfacial charge transfer resistance [91]. Fig. 4(f) presents the Nyquist plots of NiOnps, $FeWO_4$nps and NiO-$FeWO_4$ nanocomposites. A smaller arc radius signifies higher rate of separation and lower charge transfer resistance, whereas a larger arc radius corresponds to higher resistance [92]. NiOnps exhibit the smallest arc radius, consistent with its high hole mobility [27], while $FeWO_4$nps display a large arc radius, indicating poor conductivity and high resistance. The NiO-$FeWO_4$ nanocomposites show that the arc radius was smaller than $FeWO_4$nps, implying that coupling $FeWO_4$nps with NiOnps improves interfacial charge transport compared to $FeWO_4$nps alone. Amongst, NiO-*40*$FeWO_4$ shows the smallest arc radius. The combined PL and EIS results imply that heterojunction formation significantly improves charge-carrier separation in NiOnps while mitigating the charge-transfer resistance of $FeWO_4$nps, thereby addressing the inherent drawbacks of the individual pristine semiconductors.

3.3. Colloidal properties: DLS and zeta potential analysis

The particle size and polydispersity index (PDI) of NiOnps, $FeWO_4$nps, NiO-*20*$FeWO_4$, NiO-*30*$FeWO_4$, NiO-*40*$FeWO_4$, NiO-*50*$FeWO_4$ and NiO-*60*$FeWO_4$ nanocomposites are presented in Table 3. The results demonstrate the ability of CMLE as reducing agent to synthesise NiOnps (18.85 nm) and $FeWO_4$nps (9.60 nm) with smaller particle sizes

Table 3
Particle size, polydispersity index (PDI) and zeta potential of NiOnps, $FeWO_4$nps, NiO-*20*$FeWO_4$, NiO-*30*$FeWO_4$, NiO-*40*$FeWO_4$, NiO-*50*$FeWO_4$ and NiO-*60*$FeWO_4$ nanocomposites.

Sample	Particle Size (nm)	PDI	Zeta Potential (mV)
NiOnps	18.85 ± 0.6	0.294	+11.3
$FeWO_4$nps	9.60 ± 0.9	0.382	−21.7
NiO-*20*$FeWO_4$	13.37 ± 0.6	0.437	−19.2
NiO-*30*$FeWO_4$	16.96 ± 0.8	0.473	
NiO-*40*$FeWO_4$	17.53 ± 0.4	0.422	−19.0
NiO-*50*$FeWO_4$	20.02 ± 0.6	0.382	
NiO-*60*$FeWO_4$	25.66 ± 0.8	0.492	−13.4

compared to those reported using hydrothermal, sol-gel and chemical precipitation methods [11,31,84,86,87]. As shown in Fig. 5, both NiOnps and $FeWO_4$nps has a narrow particle size distribution. A PDI value of less than 0.5 suggests that the nanoparticles are monodisperse and has good colloidal stability against aggregation [93]. This observation may be attributed to flavonoids and phenolic compounds in CMLE acting as capping agents during synthesis, stabilising the nucleated NiOnps and $FeWO_4$nps and maintain the size uniformity [91,94]. The particle size and PDI value of NiO-$FeWO_4$ nanocomposites increases as the content of $FeWO_4$nps increases, which were expected in binder-assisted coupling technique for two materials with distinct phases and size [95]. Zeta potential analysis provides insights on the surface charge and colloidal stability of materials [96], where NiOnps has a positive surface charge and $FeWO_4$nps was negatively charged (Fig. S1). With increasing deposition of $FeWO_4$nps onto NiOnps, the zeta potential shifted from +11.3 to −19.2, reflecting surface charge neutralization by $FeWO_4$nps and results in enhanced suspension stability of the heterojunction nanocomposites. A comparison of particle size for NiO and $FeWO_4$ nanoparticles synthesised using CMLE and other methods are summarized in Table S1.

3.4. Surface properties: FESEM-EDX, TEM and BET analysis

The observation on physical appearance during the synthesis of NiOnps, $FeWO_4$nps and NiO-$FeWO_4$ nanocomposites, until final products were obtained, are as described in Text S4. Fig. 6 shows the morphology of NiOnps, $FeWO_4$nps, NiO-*20*$FeWO_4$, NiO-*40*$FeWO_4$, and NiO-*60*$FeWO_4$ nanocomposites, observed using FESEM at various magnifications. NiOnps exhibit a rod-like shape, which is more clearly

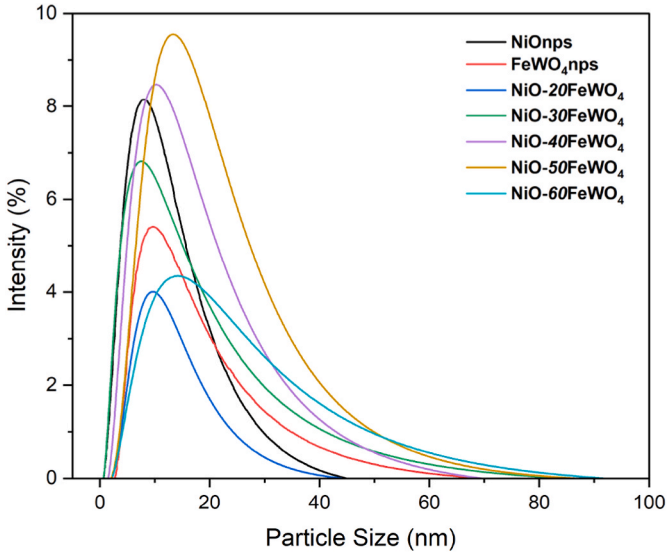

Fig. 5. Particle size distributions of NiOnps, $FeWO_4$nps, NiO-*20*$FeWO_4$, NiO-*30*$FeWO_4$, NiO-*40*$FeWO_4$, NiO-*50*$FeWO_4$ and NiO-*60*$FeWO_4$ nanocomposites.

visualised in TEM image, in Fig. 7. $FeWO_4$nps exhibit a granular morphology composed of angular and spherical shape particles. The NiO-$FeWO_4$ nanocomposites reveal a heterogeneous surface morphology composed of both fine and larger particles. It is evident that tiny $FeWO_4$nps were distributed on the surface of larger NiOnps, suggesting that $FeWO_4$nps was successfully deposited onto the surface of NiOnps. This observation is consistent with the measured particle size, tabulated in Table 4, where NiOnps exhibit larger average particle size (18.71 nm) compared to $FeWO_4$nps (9.75 nm). A clear interfacial contact between NiOnps and $FeWO_4$nps was visualised in HRTEM images. Fig. 7(d)–(f) shows the interplanar spacing was measured to be 0.21 nm and 0.22 nm, which attributed to (2 0 0) and (1 2 1) lattice planes of NiOnps and $FeWO_4$nps, respectively.

Fig. S2 displays the EDX spectra of NiOnps, $FeWO_4$nps and NiO-$FeWO_4$ nanocomposites. The EDX analysis of NiO reveals the composition of nickel (42.73 %), oxygen (42.14 %) and carbon (15.13 %). The presence of carbon might due to the residual organic matter from CMLE decomposition post-calcination, whereas the Ni and O compositions suggest stoichiometric Ni:O ratio, indicating complete oxidation of Ni $(OH)_2$ to NiO. The EDX spectrum of $FeWO_4$nps confirmed the presence of Fe, W and O, with nearly stoichiometric Fe:W (6.62:4.31) atomic ratio demonstrating high purity synthesis of $FeWO_4$nps. The weight percentage of W (31.61 %) detected was higher than Fe (14.76 %) despite its stoichiometric atomic ratio which is likely due to its larger atomic weight (W: 183.84 amu, Fe: 55.84 amu), as heavier element produces more continuum intensity [97]. The spectra of NiO-*20*$FeWO_4$, NiO-*40*-$FeWO_4$ and NiO-*60*$FeWO_4$ show a consistent increase in Fe and W content with increasing $FeWO_4$nps loading. However, the measured weight percentages of Ni, Fe and W does not exactly reflect the actual composition of NiOnps and $FeWO_4$nps in the nanocomposites. This discrepancy is likely due to peak overlaps arising from close X-ray energies of certain lines, such as between Ni L α (0.851 keV) and Fe L α (0.705 keV), as well as Ni Kα line (7.47 keV) and W Ly1 (7.39 keV). Such overlaps can influence element quantification, leading to slight overestimation or underestimation of the reported weight percentages [98]. Nonetheless, the presence of all expected elements were confirmed, supporting the successful formation of the NiO–$FeWO_4$ nanocomposites.

The N_2 adsorption-desorption isotherm of BET analysis reveals the specific surface area, pore volume and pore size of NiOnps, $FeWO_4$nps, NiO-*20*$FeWO_4$, NiO-*40*$FeWO_4$, and NiO-*60*$FeWO_4$ nanocomposites, presented in Table 4. The results show that NiOnps possesses the smallest surface area (54.15 m^2/g), whereas $FeWO_4$nps exhibit the largest surface area (126.18 m^2/g). The deposition of $FeWO_4$nps onto NiOnps significantly enhances the surface area, providing more active sites for diffusion and mass transfer of reactants [99,100]. The pore volume of all samples ranged within 3.111 to 0.4019 cm^3/g, and pore size ranging from 7.826 nm to 15.58 nm, suggesting a mesoporous material (pore size between 2 and 50 nm) [101]. As shown in Fig. S3, the isotherm curves displayed a narrow hysteresis loop (H2), with gradual filling at low P/Po followed by capillary condensation, where the characteristic matched with Type IV adsorption-desorption isotherm [102,103].

3.5. Photocatalytic degradation of methylene blue

3.5.1. Adsorption efficiency and kinetics

In photocatalysis, establishing adsorption equilibrium before light irradiation is critical, such that to assess the influence of adsorption during photocatalysis, provides a reliable baseline for kinetic calculations and ensures the MB molecules are optimally positioned near active sites for efficient photodegradation. Based on comprehensive analysis of the characterisation results, NiO-*40*$FeWO_4$ nanocomposite demonstrates optimal properties as photocatalyst for the photocatalytic degradation of MB, owing to its, narrow bandgap, low charge recombination rate, structural properties and favourable interfacial properties. The kinetics of MB adsorption on NiOnps, $FeWO_4$nps and NiO-*40*$FeWO_4$

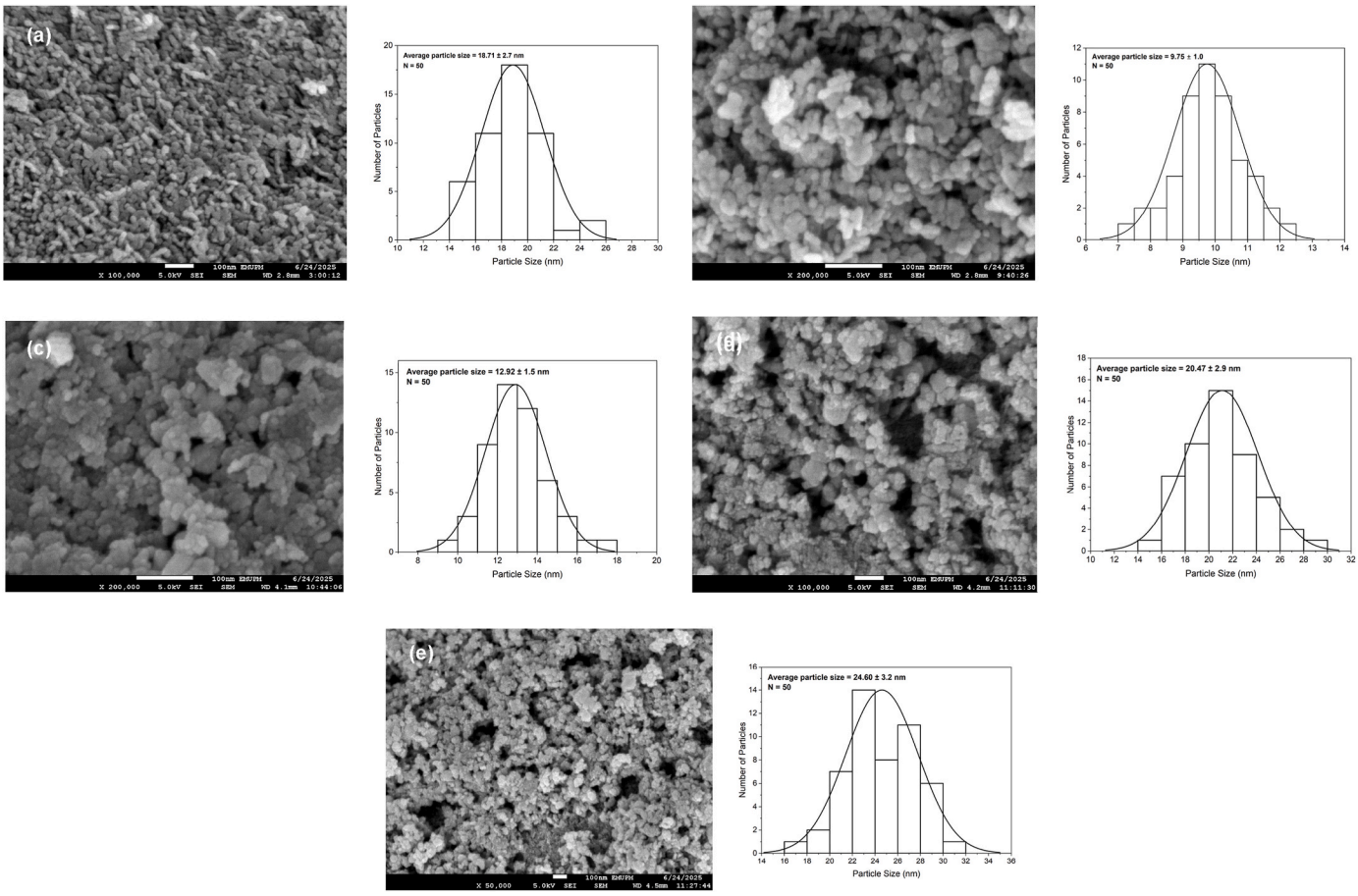

Fig. 6. FESEM images of **(a)** NiOnps, **(b)** $FeWO_4$nps, **(c)** NiO-*20*$FeWO_4$, **(d)** NiO-*40*$FeWO_4$, **(e)** NiO-*60*$FeWO_4$ nanocomposites with their particle size distributions.

nanocomposite were investigated using four kinetic models, as expressed in Equations (6)–(9) [86], respectively: pseudo-first order (PFO), pseudo-second order (PSO), Elovich and intra-particle diffusion (ID) models.

$$\ln(q_e - q_t) = \ln q_e - k_1 t \tag{6}$$

$$\frac{t}{q_t} = \frac{1}{k_2 q_e^q} + \frac{t}{q_e} \tag{7}$$

$$q_t = \frac{\ln(\alpha\beta)}{\beta} + \frac{lnt}{\beta} \tag{8}$$

$$q_t = k_i t^{\frac{1}{2}} + C_i \tag{9}$$

where q_e (mg/g) and q_t (mg/g) are the adsorption capacity at equilibrium and at time t (min), respectively. k_1 and k_2 (mg/g.min) are the rate constants for PFO and PSO, respectively. α (mg/g.min) is the initial adsorption rate and β (g/mg) is the desorption constant. k_i (mg/g.$min^{1/2}$) is the ID rate constant and C_i (mg/g) is the intercept.

Fig. 8(a) shows the adsorption efficiencies of NiOnps, $FeWO_4$nps and NiO-*40*$FeWO_4$ were 24.93 %, 31.79 % and 35.54, respectively, after reaching equilibrium (80 min). The kinetic plots are as depicted in Fig. 8 (b)–(e) and summarized in Table 5. The adsorption of MB by NiOnps was best described by ID model (R^2 = 0.9640), which suggests diffusion-controlled mechanism. In this process, rapid adsorption occurs on the surface, followed by gradual intraparticle diffusion permeating into the inner pore of NiOnps [86]. The adsorption of MB onto $FeWO_4$nps and NiO-*40*$FeWO_4$ follow the PSO model (R^2 = 0.9974 and 0.9940, respectively), indicating chemisorption-controlled process. This might be due to the electrostatic attraction between the negatively charged surfaces of $FeWO_4$nps and NiO-*40*$FeWO_4$, and positively charged MB molecules.

3.5.2. Degradation efficiency and kinetics

As presented in Fig. 9(a)–(c) and Table 6, the degradation kinetics were investigated using pseudo-first order (PFO) model and pseudo-second order (PSO) model, as expressed in Equations (10) and (11) [84,104], respectively:

$$ln\frac{C_t}{C_o} = -k_1 t \tag{10}$$

$$\frac{1}{C_t} = \frac{1}{C_o} + k_2 t \tag{11}$$

where C_t and C_o refer to MB concentration at any time, t (min) interval and initial MB concentration, respectively. k_1 (min^{-1}) and k_2 (min^{-1}) are rate constants for PFO and PSO, respectively.

The photodegradation of MB by NiOnps and NiO-*40*$FeWO_4$ nanocomposite were best described by PFO model, which indicates that the degradation of MB is driven by photogenerated electrons, holes and reactive radicals, while $FeWO_4$nps follows PSO model, implying that the degradation was governed by active-site interactions with MB molecules. Furthermore, the reaction rate constants (k) were 0.0035 min^{-1}, 0.0023 min^{-1} and 0.0496 min^{-1} for NiOnps, $FeWO_4$nps and NiO-*40*$FeWO_4$, respectively, demonstrating an efficient breakdown of MB molecules by NiO-*40*$FeWO_4$. This could be explained by the significant degradation of MB (0–20 min), upon visible light irradiation (81.3 %) compared to NiOnps (10.8 %) and $FeWO_4$nps (37.6 %). The rapid degradation might be due to the abundant photogenerated charge carriers and reactive oxygen species generated upon irradiation, which

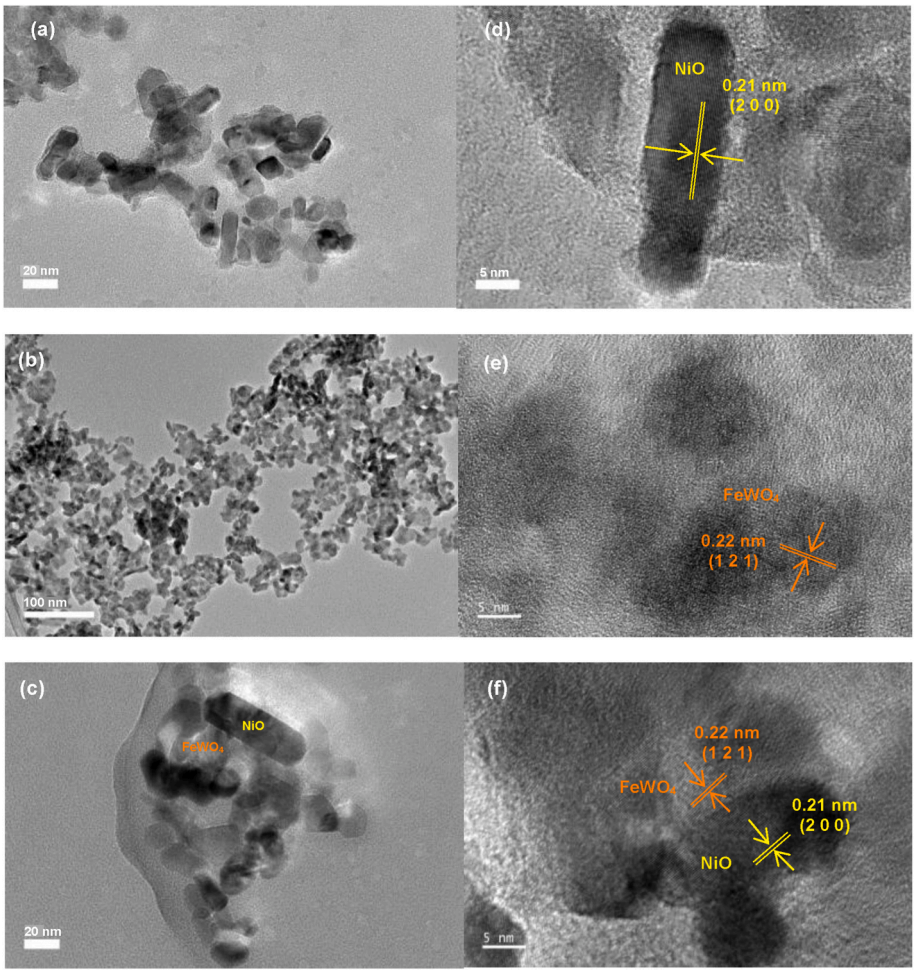

Fig. 7. (a)–(c) TEM images and **(d)–(f)** HRTEM images of NiOnps, $FeWO_4$nps and NiO-*40*$FeWO_4$ nanocomposite, respectively.

Table 4
Particle size measured using ImageJ, surface area, pore volume and pore size of NiO, $FeWO_4$nps, NiO-*20*$FeWO_4$, NiO-*40*$FeWO_4$, and NiO-*60*$FeWO_4$ nanocomposites.

Sample	Average Particle Size (nm)	Surface Area (m^2/g)	Pore Volume (cm^3/g)	Pore Size (nm)
NiOnps	18.71 ± 2.7	54.15	0.3111	15.58
$FeWO_4$nps	9.75 ± 1.0	126.18	0.4019	8.767
NiO-*20*$FeWO_4$	12.92 ± 1.5	111.86	0.3191	7.826
NiO-*40*$FeWO_4$	20.47 ± 2.9	102.62	0.3413	8.392
NiO-60FeWO4	24.60 ± 3.2	111.64	0.3334	8.902

readily react with the high local MB molecules adsorbed on the surface of NiO-*40*$FeWO_4$. As MB concentration decreases, fewer MB molecules remain in the solution and near the surface, leading to slower degradation rate (20–60 min). The NiO-*40*$FeWO_4$ nanocomposite reached equilibrium after 60 min of irradiation with 96.73 % MB degradation, while NiOnps and $FeWO_4$nps only show 21.90 % and 60.45 % degradation, respectively. This result shows that NiO-*40*$FeWO_4$ has outstanding photodegradation ability under visible light irradiation, owing to its outstanding optical properties after heterojunction formation.

The reusability of a photocatalyst is very important to evaluate its stability in practical application. Fig. 9(d) presents the reusability of NiO-*40*$FeWO_4$ nanocomposite over 4 cycles of MB photodegradation. It was observed that there was 9.13 % reduction in its efficiency, from 96.24 % to 87.11 %. This suggests that NiO-*40*$FeWO_4$ nanocomposite is a stable photocatalyst. Fig. 10 provides a clear comparison of the adsorption and photodegradation efficiencies of the photocatalysts in the removal of MB.

3.6. Proposed mechanism

To clarify the mechanism for the photodegradation of MB by the heterostructure of NiO-*40*$FeWO_4$ nanocomposite, the energy band positions of NiOnps and $FeWO_4$nps were calculated. The valence and conduction band edge potentials (E_{VB} and E_{CB}) were determined using Equations (12) and (13) [105]:

$$E_{VB} = X - E_e + 0.5E_g \quad (12)$$

$$E_{CB} = E_{VB} - E_g \quad (13)$$

where X is the absolute electronegativity (NiO = 5.04 eV, $FeWO_4$ = 5.94 eV), E_e is the energy of free electrons on the hydrogen scale (4.5 eV) and E_g is the bandgap energy obtained from Tauc plot. The calculated E_{VB} and E_{CB} for NiOnps were +1.95 eV and −0.87 eV, respectively, while those for $FeWO_4$nps were +2.45 eV and +0.44 eV.

Mott-Schottky (M − S) analysis was conducted to determine the semiconductor type and flat band potential (vs. Ag/AgCl) ($E_{FB,\ Ag/AgCl}$) of NiOnps, $FeWO_4$nps and NiO-*40*$FeWO_4$ nanocomposite. As shown in M − S plots (Fig. 11), NiOnps exhibits a negative slope, confirming its p-type semiconductor behavior, while $FeWO_4$nps shows a positive slope, indicative of an n-type semiconductor [99,106]. From the interception

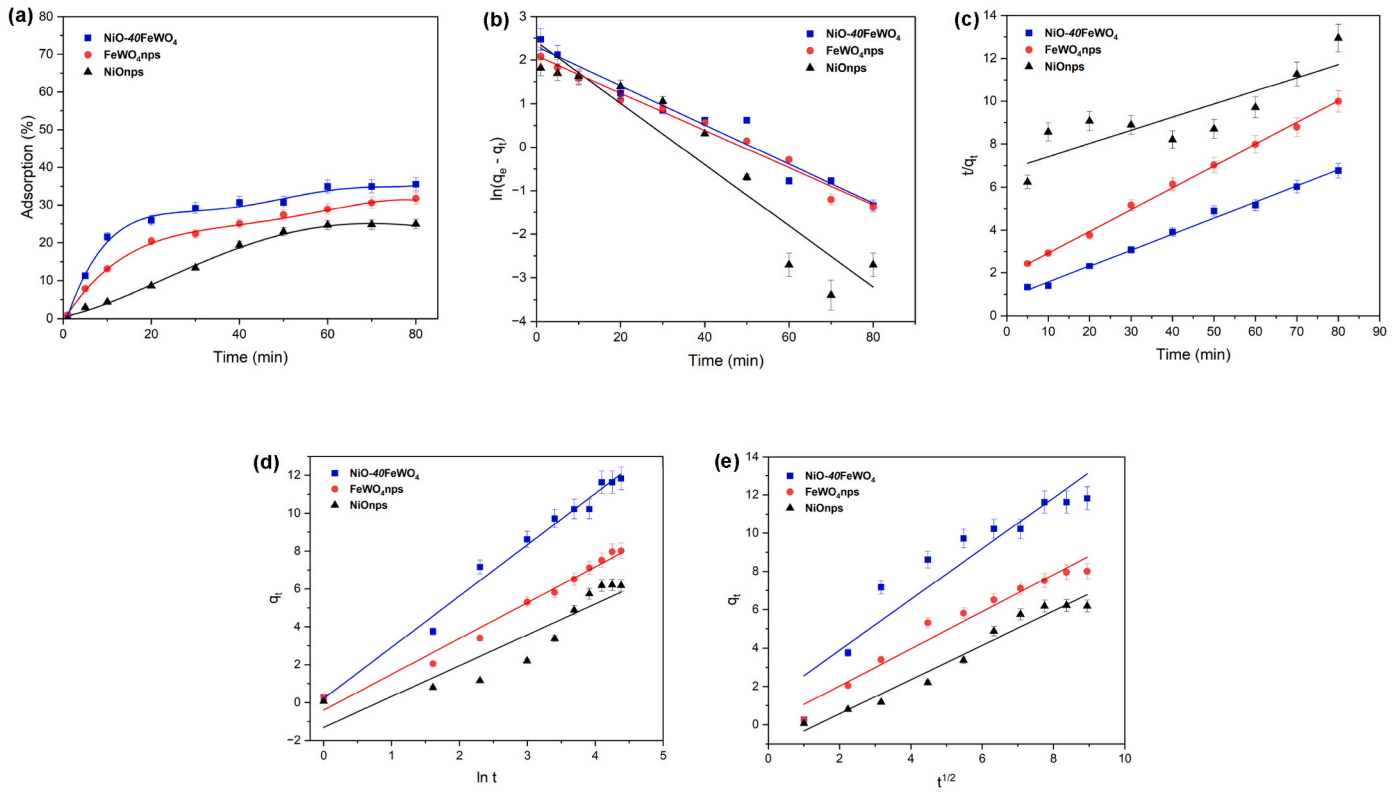

Fig. 8. **(a)** Adsorption efficiency (in the dark) and adsorption kinetic plots of NiOnps, $FeWO_4$nps and NiO-*40*$FeWO_4$ nanocomposite on MB: **b)** pseudo-first order, **c)** pseudo-second order, **d)** Elovich and **e)** intraparticle diffusion models.

Table 5
Kinetic parameters of MB adsorption on NiO, $FeWO_4$nps and NiO-*40*$FeWO_4$ nanocomposite.

Kinetic Models	Parameters	Samples		
		NiOnps	$FeWO_4$nps	NiO-*40*$FeWO_4$
PFO	R^2	0.9045	0.9818	0.957
	k_1 (min^{-1})	0.0703	0.0425	0.0434
	q_{cal} (mg/g)	11.1716	8.0393	9.2387
	q_{exp} (mg/g)	9.0848	8.2645	12.085
PSO	R^2	0.7304	0.9974	0.9940
	k_2 (g/mg.min)	0.0204	0.1001	0.0744
	q_{cal} (mg/g)	49.1302	9.9932	13.4386
	q_{exp} (mg/g)	9.0848	8.2645	12.085
Elovich	R^2	0.9296	0.9797	0.9856
	α (mg/g · min)	0.4525	0.1516	1.1973
	β (g/mg)	0.4365	1.1436	0.9425
Intra-particle Diffusion (ID)	R^2	0.9640	0.9618	0.8867
	k_i (mg/g.$min^{1/2}$)	0.5230	0.8744	1.061
	C_i (mg/g)	0.9926	0.7382	3.0766

at x-axis, the $E_{FB,\ Ag/AgCl}$ of NiOnps and $FeWO_4$nps were +1.42 eV and +0.72 eV, respectively. The $E_{FB,\ Ag/AgCl}$ values were converted to $E_{FB,\ NHE}$ using derived Nernst equation (Equation (14)) [107,108];.

$$E_{FB,NHE} = E_{FB,Ag/AgCl} + 0.24 \quad (14)$$

Thus, the $E_{FB,\ NHE}$ of NiOnps and $FeWO_4$nps were +1.66 eV and +0.96 eV, respectively. According to semiconductor energy principles, the E_{FB} for an n-type semiconductor lies ~0.2 eV below the E_{CB} and ~0.2 eV above the E_{VB} for a p-type semiconductor [106,109]. Therefore, the E_{VB} of NiOnps was determined to be +1.86 eV and E_{CB} of $FeWO_4$nps was +0.76 eV. The corresponding E_{CB} of NiOnps (−0.96 eV) and E_{VB} of $FeWO_4$nps (+2.86 eV) was calculated using Equation (13). The band edge potentials derived from M − S analysis were consistent with those calculated using empirical formula, with only minor deviations (<0.4 eV). From XPS valence band (XPS-VB) analysis (Fig. 11), the valence band potential ($E_{VB,\ XPS}$) are +1.94 eV and +2.95 eV for NiOnps and $FeWO_4$nps, respectively. The E_{VB} relative to NHE ($E_{VB,\ NHE}$) are determined using Equation (15) [92];

$$E_{VB,NHE} = \varphi + E_{VB,XPS} - 4.44 \quad (15)$$

where φ is the instrumental work function (4.47 eV). Accordingly, the $E_{VB,\ NHE}$ for NiOnps and $FeWO_4$nps are +1.97 eV and 2.98 eV, respectively. Subsequently, the corresponding E_{CB} are −0.85 eV and +0.88 eV. The band edge potentials are close with the values obtained from M − S analysis.

Fig. 12 shows the schematic illustration of energy band positions before and after junction formation. As NiOnps and $FeWO_4$nps were brought into contact, a p-n heterojunction is formed. Electrons (e^-) migrate from $FeWO_4$nps to NiOnps, while holes (h^+) migrate in the opposite direction. This bidirectional charge movement induces an internal electric field at the interface [82]. Due to the mismatch in Fermi levels (E_F), band bending occurs at the interface until E_F equilibrates, where the energy bands of NiOnps bend upwards and energy bands of $FeWO_4$nps bend downwards. Upon light irradiation, e^- from the valence band (VB) are excited to its conduction band (CB), creating h^+ in the VB. The formation of internal electric field enables the recombination of only low-energy photogenerated carriers [83], which means the e^- in the CB of $FeWO_4$nps recombine with h^+ in the VB of NiOnps, leaving behind e^- in the CB of NiOnps (−0.87 eV) and h^+ in the VB of $FeWO_4$nps (+2.45 eV), both of which possess strong redox potentials for photocatalytic reactions. The e^- in CB of NiOnps then react with dissolved O_2 molecules in the MB solution, reducing them to superoxide radicals ($\cdot O_2^-$), while the h^+ in the VB of $FeWO_4$nps oxidise H_2O to produce hydroxyl radicals ($\cdot$ OH) [110]. These reactive oxygen species subsequently attack the complex structure of MB, breaking it down into CO_2 and water. The standard redox potential for the $O_2/\cdot O_2^-$ pair is −0.33 eV and +2.34 eV for $H_2O/\cdot$ OH pair. Therefore, the conduction band electrons

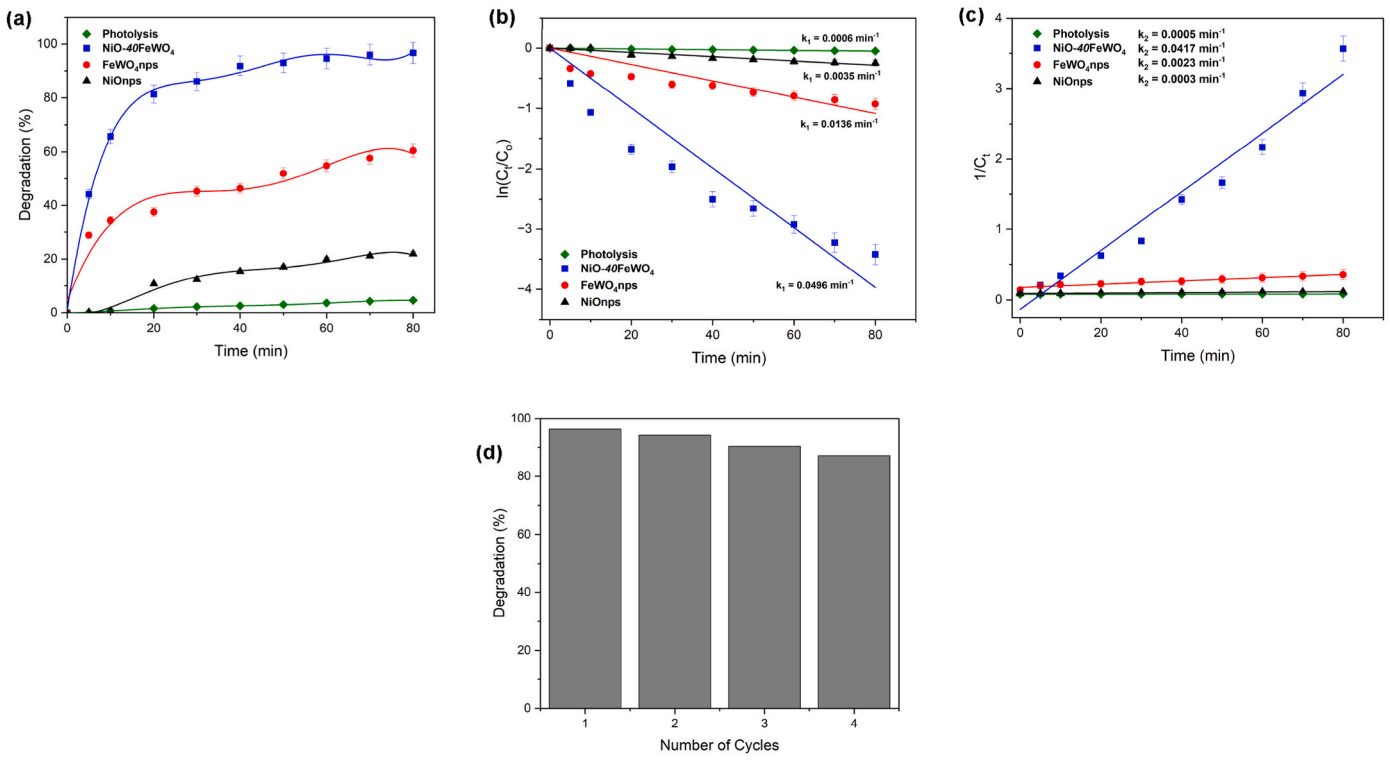

Fig. 9. **(a)** Degradation efficiency (under visible light irradiation), degradation kinetic plots of NiOnps, $FeWO_4$nps and NiO-*40*$FeWO_4$ nanocomposite on MB: **b)** pseudo-first order, **c)** pseudo-second order and **(d)** reusability of NiO-*40*$FeWO_4$ nanocomposite after four cycles.

Table 6
Kinetic parameters of MB photodegradation by NiOnps, $FeWO_4$nps and NiO-*40*$FeWO_4$ nanocomposite.

Kinetic Models	Parameters	Samples		
		NiOnps	$FeWO_4$nps	NiO-*40*$FeWO_4$
PFO	R^2	0.9767	0.9313	0.9654
	k_1 (min^{-1})	0.0035	0.0136	0.0496
PSO	R^2	0.9468	0.9538	0.9642
	k_2 (min^{-1})	0.0003	0.0023	0.0417

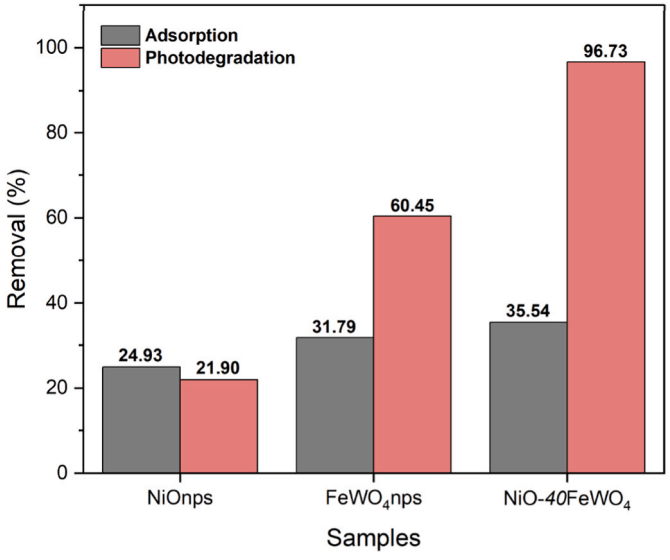

Fig. 10. Removal efficiency of MB by NiOnps, $FeWO_4$nps and NiO-*40*$FeWO_4$ nanocomposite through adsorption and photodegradation.

must possess a more negative potential than −0.33 eV to effectively reduce O_2 and more positive potential than +2.34 eV to oxidise H_2O [33]. In the NiO-*40*$FeWO_4$ heterojunction system, the CB of NiOnps and VB of $FeWO_4$nps potentials satisfy the requirements, enabling the generation of both superoxide and hydroxyl radicals. This strongly supports the operation of an S-scheme charge transfer pathway, where charge separation was enhanced while maintaining high redox capability [43, 111].

Radical scavenger experiments (Fig. 13) further validate the proposed S-scheme mechanism, as the addition of IPA (· OH scavenger) and 1,4-BQN (· O_2^- scavenger) significantly quenched the degradation efficiency of MB by NiO-*40*$FeWO_4$, from 96.73 % to 40.41 % and 18.66 %, respectively, indicating active participation of both · OH and · O_2^- in the process. This aligns with the substantial decrease upon the addition of $AgNO_3$ (e^- scavenger) (23.34 %) and EDTA (h^+ scavenger) (32.08 %) as both disrupts the redox reactions and hinder radical generation. Consistent with several reports on S-scheme heterojunctions, this charge transfer pathway efficiently promotes charge separation while preserving strong redox capability, leading to outstanding photocatalytic performance [43,92,112–114]. The following chemical equations demonstrate the proposed mechanism involved in the photodegradation of MB by NiO-*40*$FeWO_4$:

$$NiO\text{-}FeWO_4 + h\nu \rightarrow e^-_{CB} + h^+_{VB}$$

$$h^+_{VB} + H_2O \rightarrow \cdot OH + h^+$$

$$e^-_{CB} + O_2 \rightarrow O_2^-$$

$$^{\bullet}OH + MB \rightarrow \text{Degradation Products}$$

$$^{\bullet}O_2^- + MB \rightarrow \text{Degradation Products}$$

The degradation of MB molecules occurred when the highly oxidative · OH radicals attack the aromatic rings and heteroaromatic nitrogen sites of MB, initiating hydrogen abstraction and hydroxyl addition reactions that destabilise the π-conjugated system. Concurrently, · O_2^-

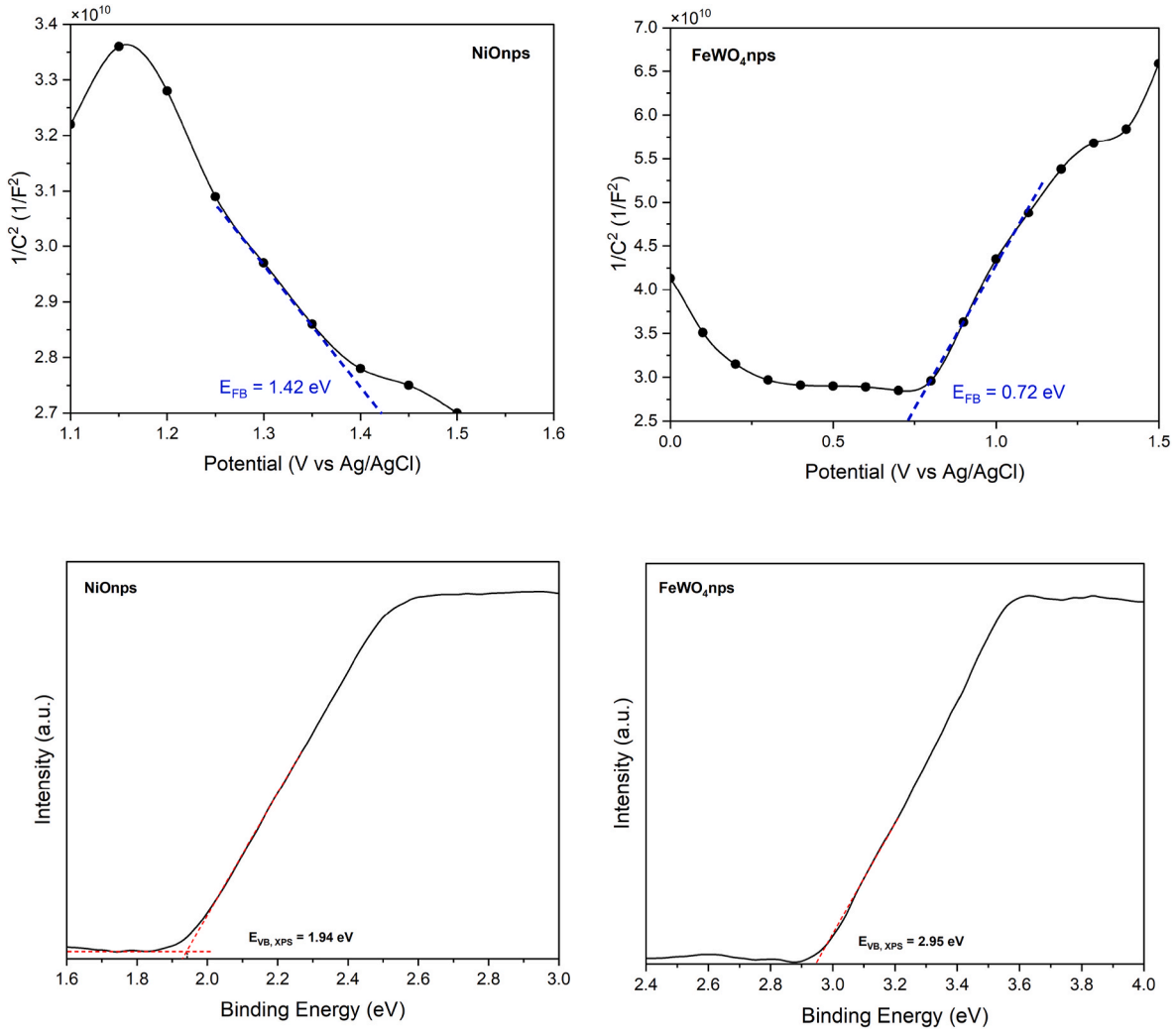

Fig. 11. **(a–b)** Mott-Schottky plots and **(c–d)** XPS-VB spectra of NiOnps and $FeWO_4$nps.

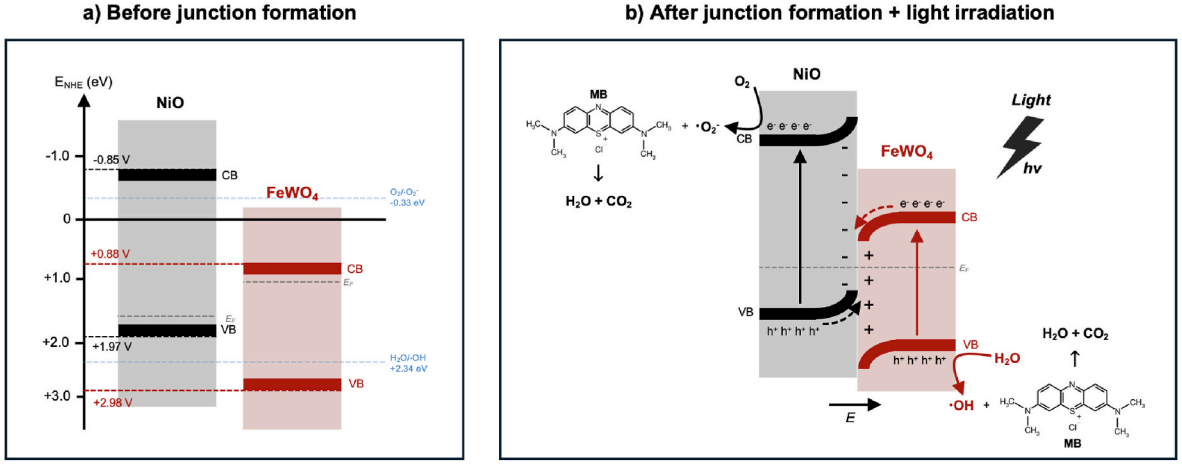

Fig. 12. Proposed schematic illustration of MB photodegradation mechanism by NiO-*40*$FeWO_4$ nanocomposite, **a)** before junction and **b)** after junction formation.

radicals undergo nucleophilic attack on the cationic MB molecules, further weakening the chromophoric C=N bonds within the phenothiazine ring structure [94]. The disruption of these bonds leads to rapid decolorization due to the breakdown of the conjugated system. Subsequent oxidative steps involve demethylation of the N-CH_3 groups and ring cleavage generating smaller aromatic intermediates, for instance 4, 4-bis(dimethylamino) benzophenone, N,N-dimethylaniline, 4-dimethylaminobenzoic acid and phenol, which were further oxidized into shorter chain of carboxylic acids and mineralized into CO_2, H_2O and inorganic ions such as NH_4^+ and SO_4^{2-} [115].

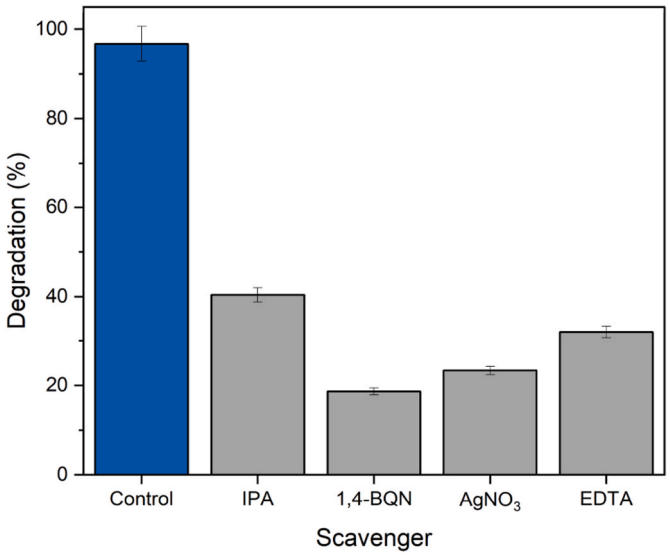

Fig. 13. Effects of different scavengers on the photocatalytic efficiency of NiO-*40*$FeWO_4$ under visible light irradiation; **Conditions:** [MB] = 10 ppm, NiO-*40*$FeWO_4$ dosage = 40 mg, pH = 7.11 (unadjusted), t = 40 min (in the dark) + 80 min (under visible light irradiation), room temperature. **Scavengers (concentration, volume)**: IPA (2 mL), 1,4-BQN (1 mM, 5 mL), $AgNO_3$ (5 mM, 5 mL) and EDTA (5 mL, 5 mM).

4. Conclusions

An S-scheme NiO-$FeWO_4$ heterojunction nanocomposite, was successfully fabricated using CMLE and PEG-200 as the molecular binder, resulting in improved structural, optical and electronic properties than pristine NiOnps and $FeWO_4$nps. The biogenic synthesis using CMLE produced rod-like NiOnps and granular $FeWO_4$nps. DLS analysis reveals the particle size of NiOnps (18.85 ± 0.6 nm) and $FeWO_4$nps (9.60 ± 0.9 nm), with low PDI values (0.382 and 0.294, respectively), validating the feasibility of CMLE as stabilising agent. Among NiO-$FeWO_4$ nanocomposites, NiO-*40*$FeWO_4$ exhibited the most favourable properties. The NiO-*40*$FeWO_4$ nanocomposite reduced the optical bandgap energy of NiOnps from 2.82 eV to 2.10 eV, suppressed PL emission of NiOnps, depleted charge transfer resistance of $FeWO_4$nps and enhanced photocurrent response of both NiOnps and $FeWO_4$nps. The coupling of NiOnps and $FeWO_4$nps successfully established an S-scheme charge transfer pathway, as evidenced by the superior photocatalytic performance of NiO-*40*$FeWO_4$ nanocomposite (96.73 % MB degradation within 80 min, under visible-light irradiation), alignment of NiOnps and $FeWO_4$nps band edge potentials and the quenching of photogenerated reactive species. Moreover, the kinetics of MB degradation with a rate constant of 0.0496 min^{-1}, far surpassing pristine NiOnps and $FeWO_4$nps. This work also demonstrates that binder-assisted physical coupling technique is capable of designing a high-performance heterojunction nanocomposite, offering a pathway for designing sustainable nanomaterials for effective wastewater remediation.

CRediT authorship contribution statement

Fatimah Lee: Writing – original draft. **Luqman Chuah Abdullah:** Writing – review & editing, Supervision. **Irmawati Ramli:** Writing – review & editing, Supervision, Resources. **Ahmad Adlie Shamsuri:** Writing – review & editing, Supervision. **Rusli Daik:** Writing – review & editing, Supervision. **Ikhwan Syafiq Mohd Noor:** Supervision, Resources. **Siti Nurul Ain Md Jamil:** Writing – review & editing, Supervision.

Declaration of competing interest

The authors declare that they have no known competing financial interests or personal relationships that could have appeared to influence the work reported in this paper.

Acknowledgements

The authors would like to thank the Department of Chemistry, Faculty of Science, Universiti Putra Malaysia, for providing the necessary facilities and support for this work. This research was funded by the Research Management Centre (RMC) of Universiti Putra Malaysia (UPM) under Geran Putra (Geran Putra Berimpak), UPM (grant code: UPM.RMC.800-3/3/1/GP-GPB/2021/9699200).

Appendix A. Supplementary data

Supplementary data to this article can be found online at https://doi.org/10.1016/j.ceramint.2025.10.220.

References

[1] P.O. Oladoye, T.O. Ajiboye, E.O. Omotola, O.J. Oyewola, Methylene blue dye: toxicity and potential elimination technology from wastewater, Results Eng. 16 (2022), https://doi.org/10.1016/j.rineng.2022.100678.
[2] P. Liang, W. Yang, H. Peng, S. Zhao, Efficient degradation of methylene blue in industrial wastewater and high cycling stability of nano ZnO, Molecules 29 (2024) 5584, https://doi.org/10.3390/molecules29235584.
[3] H. Li, V.L. Budarin, J.H. Clark, M. North, X. Wu, Rapid and efficient adsorption of methylene blue dye from aqueous solution by hierarchically porous, activated starbons®: mechanism and porosity dependence, J. Hazard Mater. 436 (2022) 129174, https://doi.org/10.1016/j.jhazmat.2022.129174.
[4] R. Al-Tohamy, S.S. Ali, F. Li, K.M. Okasha, Y.A.G. Mahmoud, T. Elsamahy, H. Jiao, Y. Fu, J. Sun, A critical review on the treatment of dye-containing wastewater: ecotoxicological and health concerns of textile dyes and possible remediation approaches for environmental safety, Ecotoxicol. Environ. Saf. 231 (2022), https://doi.org/10.1016/j.ecoenv.2021.113160.
[5] S. Dutta, S. Adhikary, S. Bhattacharya, D. Roy, S. Chatterjee, A. Chakraborty, D. Banerjee, A. Ganguly, S. Nanda, P. Rajak, Contamination of textile dyes in aquatic environment: adverse impacts on aquatic ecosystem and human health, and its management using bioremediation, J. Environ. Manag. 353 (2024), https://doi.org/10.1016/j.jenvman.2024.120103.
[6] M. Jamal, A. Awadasseid, X. Su, Exploring potential bacterial populations for enhanced anthraquinone dyes biodegradation: a critical review, Biotechnol. Lett. 44 (2022) 1011–1025, https://doi.org/10.1007/s10529-022-03279-2.
[7] E.R. Kenawy, H. Tenhu, S.A. Khattab, A.A. Eldeeb, M.M. Azaam, Highly efficient adsorbent material for removal of methylene blue dye based on functionalized polyacrylonitrile, Eur. Polym. J. 169 (2022), https://doi.org/10.1016/j.eurpolymj.2022.111138.
[8] U. Hübner, S. Spahr, H. Lutze, A. Wieland, S. Rüting, W. Gernjak, J. Wenk, Advanced oxidation processes for water and wastewater treatment – guidance for systematic future research, Heliyon 10 (2024) e30402, https://doi.org/10.1016/j.heliyon.2024.e30402.
[9] F. Mansouri, K. Chouchene, N. Roche, M. Ksibi, Removal of pharmaceuticals from water by adsorption and advanced oxidation processes: state of the art and trends, Appl. Sci. 11 (2021), https://doi.org/10.3390/app11146659.
[10] Y.S. Kuo, M.J. Lin, C.L. Hsu, Y.H. Liu, Heterostructured YFeO3/CeO2 as efficient photoelectrode for photoelectrochemical degradation of organic pollutants under visible light irradiation, J. Water Proc. Eng. 56 (2023), https://doi.org/10.1016/j.jwpe.2023.104394.
[11] M. Irfan, N. Tahir, M. Zahid, S. Noreen, M. Yaseen, M. Shahbaz, G. Mustafa, R. A. Shakoor, I. Shahid, The fabrication of halogen-doped FeWO4 heterostructure anchored over graphene oxide nanosheets for the sunlight-driven photocatalytic degradation of methylene blue dye, Molecules 28 (2023), https://doi.org/10.3390/molecules28207022.
[12] M.S. Khosrowshahi, S.A. Hariri, M. Rahimi, H.B.M. Emrooz, F. Shemirani, Green synthesis of a ZnO/ZnS-decorated magnetic porous carbon hybrid for enhanced rhodamine B adsorption and photodegradation: a combined DFT and experimental study, Sustain. Mater. Technol. 43 (2025), https://doi.org/10.1016/j.susmat.2024.e01231.
[13] I. Khan, C. Wang, S. Khan, J. Chen, A. Khan, S.A. Shah, A. Yuan, S. Khan, M. K. Butt, H. Asghar, Bio-capped and green synthesis of ZnO/g-C3N4 nanocomposites and its improved antibiotic and photocatalytic activities: an exceptional approach towards environmental remediation, Chin. J. Chem. Eng. 56 (2023) 215–224, https://doi.org/10.1016/j.cjche.2022.07.031.
[14] R.I. Ashna, Y. Yulizar, D.O.B. Apriandanu, Strobilanthes crispus (B.) leaf extract-assisted green synthesis of ZnO-La2O3 composite and preliminary study of its photocatalytic activity, in: IOP Conf Ser Mater Sci Eng, Institute of Physics Publishing, 2020, https://doi.org/10.1088/1757-899X/763/1/012004.

[15] M. Rezaei, A. Nezamzadeh-Ejhieha, The ZnO-NiO nano-composite: a brief characterization, kinetic and thermodynamic study and study the arrhenius model on the sulfasalazine photodegradation, Int. J. Hydrogen Energy 45 (2020) 24749–24764, https://doi.org/10.1016/j.ijhydene.2020.06.258.

[16] Z. Liu, X. Yu, K. Wang, Y. Wei, J. Zhang, J. Niu, Construction of SnO2/Cu2O heterojunctions for enhanced photocatalytic degradation of moxifloxacin, Vacuum 230 (2024), https://doi.org/10.1016/j.vacuum.2024.113669.

[17] H. Derikvandi, A. Nezamzadeh-Ejhieh, Synergistic effect of p-n heterojunction, supporting and zeolite nanoparticles in enhanced photocatalytic activity of NiO and SnO2, J. Colloid Interface Sci. 490 (2017) 314–327, https://doi.org/10.1016/j.jcis.2016.11.069.

[18] L. Gnanasekaran, R. Hemamalini, R. Saravanan, K. Ravichandran, F. Gracia, S. Agarwal, V.K. Gupta, Synthesis and characterization of metal oxides (CeO2, CuO, NiO, Mn3O4, SnO2 and ZnO) nanoparticles as photo catalysts for degradation of textile dyes, J. Photochem. Photobiol., B 173 (2017) 43–49, https://doi.org/10.1016/j.jphotobiol.2017.05.027.

[19] L. Yadeta Gemachu, A. Lealem Birhanu, Green synthesis of ZnO, CuO and NiO nanoparticles using neem leaf extract and comparing their photocatalytic activity under solar irradiation, Green Chem. Lett. Rev. 17 (2024), https://doi.org/10.1080/17518253.2023.2293841.

[20] N. Tamam, M. Aadil, W. Hassan, S.R. Ejaz, Z.M. Najm, I.A. Alsafari, S. Aman, A. V Trukhanov, M.S. Al-Buriahi, I. Boukhris, Surfactant assisted synthesis of nanostructured Mn-doped CuO: an efficient photocatalyst for environmental remediation, Ceram. Int. 48 (2022) 29589–29600, https://doi.org/10.1016/j.ceramint.2022.06.213.

[21] H. Chang, E.H. Jo, H.D. Jang, T.O. Kim, Synthesis of PEG-modified TiO2-InVO4 nanoparticles via combustion method and photocatalytic degradation of methylene blue, Mater. Lett. 92 (2013) 202–205, https://doi.org/10.1016/j.matlet.2012.11.006.

[22] L.I. Jinga, G. Popescu-Pelin, G. Socol, S. Mocanu, M. Tudose, D.C. Culita, A. Kuncser, P. Ionita, Chemical degradation of methylene blue dye using tio2/au nanoparticles, Nanomaterials 11 (2021), https://doi.org/10.3390/nano11061605.

[23] S.M. Pasini, A. Valério, G. Yin, J. Wang, S.M.A.G.U. de Souza, D. Hotza, A.A.U. de Souza, An overview on nanostructured TiO2–containing fibers for photocatalytic degradation of organic pollutants in wastewater treatment, J. Water Proc. Eng. 40 (2021), https://doi.org/10.1016/j.jwpe.2020.101827.

[24] R. Solano, D. Maestre, M. Mueses, A. Herrera, TiO2-CuO heterojunction nanoparticles synthesized by green chemistry supported on beach sand granules: optical, morphological and structural characterization, Nano-Struct. Nano-Objects 35 (2023), https://doi.org/10.1016/j.nanoso.2023.101024.

[25] H. Boudghene Stambouli, F. Guenfoud, A. Benomara, M. Mokhtari, M. Sönmez-Çelebi, Synthesis of FeWO4 heterogeneous composite by the sol–gel process: enhanced photocatalytic activity on malachite green, React. Kinet. Mech. Catal. 133 (2021) 563–578, https://doi.org/10.1007/s11144-021-01994-x.

[26] M.A. Ahmed, M.A. Ahmed, A.A. Mohamed, Fabrication of NiO/g-C3N4 Z-scheme heterojunction for enhanced photocatalytic degradation of methylene blue dye, Opt. Mater. 151 (2024), https://doi.org/10.1016/j.optmat.2024.115339.

[27] M. Ashfaq, A. Ali, N.K. Abbood, S. Panchal, N. Akram, M. Saeed, O.P. Doshi, F. Ali, S. Muhammad, M.Y. Sameeh, A.N. Nazar, Enhanced photocatalytic activity of the Bi2O3-NiO heterojunction for the degradation of methyl Orange under irradiation of sunlight, Water (Switzerland) 15 (2023), https://doi.org/10.3390/w15183182.

[28] J. Li, H. Liu, Z. Liu, D. Yang, M. Zhang, L. Gao, Y. Zhou, C. Lu, Facile synthesis of Z-scheme NiO/α-MoO3 p-n heterojunction for improved photocatalytic activity towards degradation of methylene blue, Arab. J. Chem. 15 (2022), https://doi.org/10.1016/j.arabjc.2021.103513.

[29] Zia-ul-Mustafa, K. Javaid, R. Anjum, A. Ali, K. Mahmood, N. Amin, M.S. Al-Buriahi, K.M. Katubi, Z.A. Alrowaili, U. Shehzad, H. Anwar, M. Saleem, Z. Rasheed, H. Waheed, Z. Afzal, M.Y. Ali, Band offset engineering to improve electrical transport properties of p-NiO/n-ZnO heterojunction diode, J. Alloys Compd. 1018 (2025), https://doi.org/10.1016/j.jallcom.2025.179281.

[30] E.F.A. Zeid, I.A. Ibrahem, A.M. Ali, W.A.A. Mohamed, The effect of CdO content on the crystal structure, surface morphology, optical properties and photocatalytic efficiency of p-NiO/n-CdO nanocomposite, Results Phys. 12 (2019) 562–570, https://doi.org/10.1016/j.rinp.2018.12.009.

[31] Y. Shuai, R. Peng, Y. He, X. Liu, X. Wang, W. Guo, NiO/BiVO4 p-n heterojunction microspheres for conductometric triethylamine gas sensors, Sensor. Actuator. B Chem. 384 (2023), https://doi.org/10.1016/j.snb.2023.133625.

[32] N.T.T. Vo, S.J. You, M.T. Pham, V. Van Pham, A green synthesis approach of p-n CuO/ZnO junctions for multifunctional photocatalysis towards the degradation of contaminants, Environ. Technol. Innov. 32 (2023), https://doi.org/10.1016/j.eti.2023.103285.

[33] D. Salazar-Marín, G. Oza, J.A.D. Real, A. Cervantes-Uribe, H. Pérez-Vidal, M. K. Kesarla, J.G.T. Torres, S. Godavarthi, Distinguishing between type II and S-scheme heterojunction materials: a comprehensive review, Appl. Surf. Sci. Adv. 19 (2024), https://doi.org/10.1016/j.apsadv.2023.100536.

[34] A.K. Chakraborty, S. Akter, S. Ganguli, M.A. Haque, A.S.M. Nur, M.A. Sabur, Design of FeWO4@N-TiO2 nanocomposite and its enhanced photocatalytic activity in decomposing methylene blue and phenol under visible light, Environ. Technol. Innov. 33 (2024), https://doi.org/10.1016/j.eti.2024.103536.

[35] G. Tekin, G. Ersöz, S. Atalay, Comparison of synthesis methods for BiOI/g-C3N4 heterojunction photocatalysts and testing their visible light activity in sugar processing wastewater treatment, J. Ind. Eng. Chem. 126 (2023) 292–306, https://doi.org/10.1016/j.jiec.2023.06.020.

[36] S. Wu, M. Xu, L. Ai, Q. Ma, C. Leng, N. Guo, H. Fan, L. Wang, Reasonable construction of BiOBr/Bi-MOF S-scheme heterojunction in situ introduced by Bi-MOF for efficient photocatalytic reduction of CO2 to CO, J. Colloid Interface Sci. (2025) 138807, https://doi.org/10.1016/j.jcis.2025.138807.

[37] A. Khane, N. Tahmasebi, H.S. Kaboli, PVP-assisted hydrothermal synthesis of BiOCl/Bi2Mo3O12 photocatalyst for decolorization of rhodamine B under visible-light irradiation, Kor. J. Chem. Eng. 39 (2022) 1248–1256, https://doi.org/10.1007/s11814-021-1042-7.

[38] T.N. Shulha, M. Serdechnova, S.V. Lamaka, D.C.F. Wieland, K.N. Lapko, M. L. Zheludkevich, Chelating agent-assisted in situ LDH growth on the surface of magnesium alloy, Sci. Rep. 8 (2018), https://doi.org/10.1038/s41598-018-34751-7.

[39] S. Sowndharya, M. Nikitha, S. Meenakshi, Designing an in-situ embedment of citric acid@HAp/ZnO as a Z-scheme heterojunction for substantial enhancement in photocatalytic degradation of malachite green under visible light, J. Clean. Prod. 490 (2025) 144723, https://doi.org/10.1016/j.jclepro.2025.144723.

[40] A. Sharma, N. Liu, Q. Ma, H. Zheng, N. Kawazoe, G. Chen, Y. Yang, PEG assisted P/Ag/Ag2O/Ag3PO4/TiO2 photocatalyst with enhanced elimination of emerging organic pollutants in salinity condition under solar light illumination, Chem. Eng. J. 385 (2020), https://doi.org/10.1016/j.cej.2019.123765.

[41] A.M. Fallatah, S. Aman, H.M.T. Farid, Facile hydrothermally synthesized 2D-Based rGO/NiO nanohybrid for environmental remediation of malachite green pollutant, Kor. J. Chem. Eng. 41 (2024) 503–513, https://doi.org/10.1007/s11814-024-00083-8.

[42] M.M. Ba-Abbad, M.S. Takriff, A. Benamor, A.W. Mohammad, Size and shape controlled of α-Fe2O3 nanoparticles prepared via sol–gel technique and their photocatalytic activity, J. Sol. Gel Sci. Technol. 81 (2017) 880–893, https://doi.org/10.1007/s10971-016-4228-4.

[43] W.T. Alsaggaf, R.M. Mohamed, Constructing a robust mesoporous S-scheme heterojunction AgVO3/ZnWO4 for visible-light-driven oxidation of atrazine, Ceram. Int. (2025), https://doi.org/10.1016/j.ceramint.2025.06.252.

[44] Q. Duan, F. Kong, X. Han, Y. Jiang, T. Liu, Y. Chang, L. Zhou, G. Qin, X. Zhang, Synthesis and characterization of morphology-controllable BiFeO3 particles with efficient photocatalytic activity, Mater. Res. Bull. 112 (2019) 104–108, https://doi.org/10.1016/j.materresbull.2018.12.012.

[45] M.L. Herrera-Mares, B.A. Jiménez-López, R. Leyva-Ramos, A. Jacobo-Azuara, J. Rodríguez-Hernández, R.D. Peralta-Rodríguez, I.R. Galindo-Esquivel, E. Mendoza-Mendoza, Novel p-ZnCo2O4/n-Bi2WO6 heterojunctions for efficient rhodamine B and tetracycline photodegradation, and Cr(VI) photoreduction under visible LED and sunlight irradiation, Ceram. Int. 51 (2025) 9209–9223, https://doi.org/10.1016/j.ceramint.2024.12.355.

[46] A. Vinukonda, N. Bolledla, R.K. Jadi, R. Chinthala, V.R. Devadasu, Synthesis of nanoparticles using advanced techniques, Nanotechnology 8 (2025), https://doi.org/10.1016/j.nxnano.2025.100169.

[47] N.P.U. Nguyen, N.T. Dang, L. Doan, T.T.H. Nguyen, Synthesis of silver nanoparticles: from conventional to 'modern' methods—A review, Processes 11 (2023), https://doi.org/10.3390/pr11092617.

[48] G. Taka, T.D. Das, Synthesis of ZnO nanoparticles through a simple wet chemical precipitation method, in: IOP Conf Ser Earth Environ Sci, Institute of Physics, 2022, https://doi.org/10.1088/1755-1315/1042/1/012017.

[49] S. Ying, Z. Guan, P.C. Ofoegbu, P. Clubb, C. Rico, F. He, J. Hong, Green synthesis of nanoparticles: current developments and limitations, Environ. Technol. Innov. 26 (2022) 102336, https://doi.org/10.1016/j.eti.2022.102336.

[50] S. Ayyanaar, M.P. Kesavan, One-pot biogenic synthesis of gold nanoparticles@saponins niosomes: sustainable nanomedicine for antibacterial, anti-inflammatory and anticancer therapeutics, Colloids Surf. A Physicochem. Eng. Asp. 676 (2023), https://doi.org/10.1016/j.colsurfa.2023.132229.

[51] B. Mickky, H. Elsaka, M. Abbas, A. Gebreil, R. Shams Eldeen, Orange peel-mediated synthesis of silver nanoparticles with antioxidant and antitumor activities, BMC Biotechnol. 24 (2024), https://doi.org/10.1186/s12896-024-00892-z.

[52] M. Ohiduzzaman, M.N.I. Khan, K.A. Khan, B. Paul, Biosynthesis and characterizations of silver nanoparticles by using green banana peel extract: evaluation of their antibacterial and electrical performances, Heliyon 10 (2024) e31140, https://doi.org/10.1016/j.heliyon.2024.e31140.

[53] C. Pechyen, K. Ponsanti, B. Tangnorawich, N. Ngernyuang, Waste fruit peel – mediated green synthesis of biocompatible gold nanoparticles, J. Mater. Res. Technol. 14 (2021) 2982–2991, https://doi.org/10.1016/j.jmrt.2021.08.111.

[54] M.J.K. Ahmed, M. Ahmaruzzaman, M.H. Bordoloi, Novel Averrhoa carambola extract stabilized magnetite nanoparticles: a green synthesis route for the removal of chlorazol Black e from wastewater, RSC Adv. 5 (2015) 74645–74655, https://doi.org/10.1039/c5ra13970h.

[55] P. Sathiya, K. Geetha, Fruit extract mediated synthesis of silver oxide nanoparticles using *Dimocarpus longan* fruit and their assesment of catalytic, antifungal, antioxidant and cytotoxic potentials, Inorg. Nano-Metal Chem. 53 (2023) 1173–1183, https://doi.org/10.1080/24701556.2021.1983834.

[56] M. Malakootian, S.N. Asadzadeh, M. Mehdipoor, D. Kalantar-Neyestanaki, N. Firouzeh, Stevia rebaudiana leaf extract mediated green synthesis of cerium oxide nanoparticles for antibacterial activity and photocatalytic degradation of tetracycline, Desalination Water Treat. 317 (2024), https://doi.org/10.1016/j.dwt.2024.100126.

[57] P. Nepal, S. Parajuli, G.P. Awasthi, K.P. Sharma, H.B. Oli, R.L. Shrestha, D. P. Bhattarai, Eco-friendly synthesis of cuo@zno nanocomposites using Artemisia vulgaris leaf extract and study of its photocatalytic activity for methylene blue, J. Nanotechnol. 2024 (2024) 1–15, https://doi.org/10.1155/2024/6896986.

[58] S. kazemi, A. Hosseingholian, S.D. Gohari, F. Feirahi, F. Moammeri, G. Mesbahian, Z.S. Moghaddam, Q. Ren, Recent advances in green synthesized nanoparticles: from production to application, Mater. Today Sustain. 24 (2023), https://doi.org/10.1016/j.mtsust.2023.100500.
[59] J. Zhang, Q. Wang, H. Yu, L. Lin, Z. Zhang, Y. Song, Metagenomic insights into protein degradation mechanisms in natural fermentation of cassava leaves, Bioresour. Technol. 396 (2024), https://doi.org/10.1016/j.biortech.2024.130433.
[60] C. Grella Miranda, P. Speranza, A. Carla Kawazoe Sato, Cassava leaves as an alternative protein source: effect of alkaline parameters and precipitation conditions on protein extraction and recovery, Food Res. Int. 192 (2024), https://doi.org/10.1016/j.foodres.2024.114807.
[61] A. Mukhtar, S. Latif, Z. Barati, J. Müller, Valorization of cassava by-products: cyanide content and quality characteristics of leaves and peel, Appl. Sci. 13 (2023), https://doi.org/10.3390/app13106340.
[62] M. Rashid, H.M. Aboshady, Y.A. Soltan, H. Archimede, W.M.A. Ghoneem, Phytochemical profile and in vitro evaluation of cassava (Manihot esculenta Crantz) foliage as ruminant feed with/without green banana flour, Sci. Rep. 15 (2025), https://doi.org/10.1038/s41598-024-82450-3.
[63] M. Majithia, D.A. Barretto, Biocompatible green-synthesized nanomaterials for therapeutic applications, in: Advances in Nano and Biochemistry: Environmental and Biomedical Applications, Elsevier, 2023, pp. 285–367, https://doi.org/10.1016/B978-0-323-95253-8.00012-7.
[64] T. Alomayri, Enhanced interfacial charge transfer in BiVO4/rGO/FeVO4 heterojunction composite for improved photocatalysis water purification, Ceram. Int. 51 (2025) 10193–10199, https://doi.org/10.1016/j.ceramint.2024.12.450.
[65] A. Gola, M. Kozłowska, W. Musiał, Influence of the poly(ethylene glycol) methyl ether methacrylates on the selected physicochemical properties of thermally sensitive polymeric particles for controlled drug delivery, Polymers 14 (2022), https://doi.org/10.3390/polym14214729.
[66] Z. Sabouri, A. Akbari, H.A. Hosseini, M. Khatami, M. Darroudi, Green-based bio-synthesis of nickel oxide nanoparticles in Arabic gum and examination of their cytotoxicity, photocatalytic and antibacterial effects, Green Chem. Lett. Rev. 14 (2021) 402–412, https://doi.org/10.1080/17518253.2021.1923824.
[67] W. Zhu, Y. Wang, J. Chen, Y. Liu, Q. Qiu, J. Zeng, T. Liang, Construction of Bi2S3/FeWO4 Z-Scheme heterojunction for efficient photo-Fenton degradation of antibiotics: performance and degradation mechanism, J. Environ. Chem. Eng. 12 (2024), https://doi.org/10.1016/j.jece.2024.113926.
[68] H.B. Modolon, J. Inocente, A.M. Bernardin, O.R. Klegues Montedo, S. Arcaro, Nanostructured biological hydroxyapatite from Tilapia bone: a pathway to control crystallite size and crystallinity, Ceram. Int. 47 (2021) 27685–27693, https://doi.org/10.1016/j.ceramint.2021.06.193.
[69] Z. Cheng, X. Wang, J. Gao, M. Wang, A. Wang, H. Bo, Z. Guo, W. Zou, X. Ma, Deposition and structural investigation of uniform AlN(100) films at wafer scale through RF magnetron sputtering, Ceram. Int. 50 (2024) 28601–28608, https://doi.org/10.1016/j.ceramint.2024.05.170.
[70] T. Feng, R. Pinal, M.T. Carvajal, Process induced disorder in crystalline materials: differentiating defective crystals from the amorphous form of griseofulvin, J. Pharmacol. Sci. 97 (2008) 3207–3221, https://doi.org/10.1002/jps.21219.
[71] S. Dolabella, A. Borzì, A. Dommann, A. Neels, Lattice strain and defects analysis in nanostructured semiconductor materials and devices by high-resolution X-Ray diffraction: theoretical and practical aspects, Small Methods 6 (2022), https://doi.org/10.1002/smtd.202100932.
[72] J. Luo, K. Wang, Y. Qiu, X. Zhou, X. Ning, L. Zhan, X. Zhou, Built-in electric field mediated S-scheme high-quality charge separation in BiVO4/NiAl-LDH heterojunction for highly efficient photocatalytic degradation of antibiotics, J. Alloys Compd. 1008 (2024), https://doi.org/10.1016/j.jallcom.2024.176572.
[73] C. Xia, Y. Zheng, Y. Chu, J. Xu, R. Dong, L. Zhuang, L. Zhao, Y. He, Construction of 0D/2D Ag2S/CoAl-LDH S-scheme heterojunction for enhanced photocatalytic nitrogen fixation, J. Environ. Chem. Eng. 13 (2025), https://doi.org/10.1016/j.jece.2025.117869.
[74] J. Luo, X. Zhou, F. Yang, X. Ning, L. Zhan, Z. Wu, X. Zhou, Generating a captivating S-scheme CuBi2O4/CoV2O6 heterojunction with boosted charge spatial separation for efficiently removing tetracycline antibiotic from wastewater, J. Clean. Prod. 357 (2022), https://doi.org/10.1016/j.jclepro.2022.131992.
[75] J. Lu, Y. Lu, P. Rosaiah, S. Lin, Z. Amir, K. Qi, ZnCo2O4-ZnO S-Scheme heterojunction for photocatalytic degradation of cefalexin and antimicrobial properties, Chem. Res. Chin. Univ. 41 (2025) 799–811, https://doi.org/10.1007/s40242-025-5089-6.
[76] C. Li, S. Lin, W. Zhang, K. Qi, Enhanced photocatalytic degradation of tetracycline by mn,s co-doped TiO2 under visible-light irradiation, J. Photochem. Photobiol. Chem. 467 (2025), https://doi.org/10.1016/j.jphotochem.2025.116423.
[77] X. Zhou, Z. Liang, Z. Wu, X. Zhou, X. Ning, L. Zhan, J. Luo, Reasonably constructing BiVO4/CoNiFe-LDH S-scheme heterojunction with fast interface charge transfer for efficient photodegradation of tetracycline, Adv. Powder Technol. 36 (2025), https://doi.org/10.1016/j.apt.2025.104858.
[78] S. yuan Liu, S. Dong, Y. Hao, K. Qi, A. Peng, Gd-doped ZnFe2O4 multi-shell microspheres for enhancing photocatalytic H2 production or antibiotic degradation, J. Rare Earths 43 (2025) 1412–1420, https://doi.org/10.1016/j.jre.2024.06.035.
[79] Z. Jiang, C. Pan, D. Xu, Z. Yan, H. Zhang, F. Zhang, J. Yang, Z. Tu, X. Bai, The heterojunction of NiO/MgFe-LDH promoted degradation of nitrogenous disinfection by-products in electrochemical system via accelerating singlet oxygen generation, Sep. Purif. Technol. 354 (2025), https://doi.org/10.1016/j.seppur.2024.128684.
[80] B. Tan, J. Yan, X. Cao, Z. Song, Enhanced photocatalytic degradation of organic pollutants using Z-scheme CN/WO3 composites under visible light irradiation, Ceram. Int. 51 (2025) 23857–23864, https://doi.org/10.1016/j.ceramint.2025.03.074.
[81] T. Gul, S. Ahmad, I. Khan, I. Khan, M. Almehmadi, A. Amer Alsaiari, M. Allahyani, K. Saeed, Photodegradation of orange II dye using p-n junction NiO/TiO2 composite, and assessment of its biological activities, J. Saudi Chem. Soc. 27 (2023), https://doi.org/10.1016/j.jscs.2023.101654.
[82] X. Wang, L. Ge, K. Wei, Z. Xing, S. Feng, Fabrication of S-scheme Zn1-xCdxS/NiO heterojunction for efficient photocatalytic hydrogen evolution, Int. J. Hydrogen Energy 55 (2024) 718–728, https://doi.org/10.1016/j.ijhydene.2023.10.170.
[83] V. Soni, Sonu, P. Singh, S. Thakur, T. Ahamad, V.H. Nguyen, V. Chaudhary, N. Kumar, S. Kaya, C.M. Hussain, P. Raizada, Oxygen vacancy enriched SrTiO3 and NiO-based S-scheme heterojunction moored on activated carbon from exhausted water filter batteries for ameliorated photodegradation of doxycycline hydrochloride and methyl orange degradation, J. Taiwan Inst. Chem. Eng. 159 (2024), https://doi.org/10.1016/j.jtice.2024.105419.
[84] A. Aridi, D. Naoufal, H. El-Rassy, R. Awad, Photocatalytic activity of ZnFe2O4/NiO nanocomposites carried out under UV irradiation, Ceram. Int. 48 (2022) 30905–30916, https://doi.org/10.1016/j.ceramint.2022.07.046.
[85] K. Kato, S. Vaucher, P. Hoffmann, Y. Xin, T. Shirai, A novel single-mode microwave assisted synthesis of metal oxide as visible-light photocatalyst, Mater. Lett. 235 (2019) 125–128, https://doi.org/10.1016/j.matlet.2018.09.132.
[86] H. Far, M. Hamici, M. Ghemid, K. Haddadi, N. Brihi, Synergistic photocatalytic performance of n-Fe2O3/p-NiO heterojunctions under visible light, Mater. Sci. Eng., B 310 (2024), https://doi.org/10.1016/j.mseb.2024.117717.
[87] F. Wang, W. Li, S. Gu, H. Li, X. Liu, M. Wang, Fabrication of FeWO4@ZnWO4/ZnO heterojunction photocatalyst: synergistic effect of ZnWO4/ZnO and FeWO4@ZnWO4/ZnO heterojunction structure on the enhancement of visible-light photocatalytic activity, ACS Sustain. Chem. Eng. 4 (2016) 6288–6298, https://doi.org/10.1021/acssuschemeng.6b00660.
[88] R.K. Santos, T.A. Martins, G.N. Silva, M.V.S. Conceição, I.C. Nogueira, E. Longo, G. Botelho, Ag3PO4/NiO composites with enhanced photocatalytic activity under visible light, ACS Omega 5 (2020) 21651–21661, https://doi.org/10.1021/acsomega.0c02456.
[89] J. Xu, X. Yan, X. Reng, R. Dong, Y. Chu, Y. Zheng, K. Wang, Y. Wu, Y. He, Ultrasound-driven S-scheme g-C3N5/Bi4Ti3O12 heterojunctions for enhanced piezocatalytic degradation of organic dyes, J. Environ. Chem. Eng. 13 (2025) 118386, https://doi.org/10.1016/j.jece.2025.118386.
[90] Y. Zheng, Y. Chu, R. Dong, J. Xu, L. Zhao, K. Wang, Y. Wu, Y. He, Stepwise hydrothermal synthesis of Bi2S3/PbBiO2Cl S-scheme heterojunction for synergistic piezo-photocatalytic dyes degradation, J. Alloys Compd. 1037 (2025), https://doi.org/10.1016/j.jallcom.2025.182237.
[91] J. Zhan, L. Liang, Y. Lu, S. Jiang, G. Imanova, S. Komarneni, J. Ma, Z-scheme heterojunction photocatalyst of LaFeO3@CoS for tetracycline hydrochloride degradation by persulfate activation using visible light, Ceram. Int. 51 (2025) 1081–1095, https://doi.org/10.1016/j.ceramint.2024.11.090.
[92] Y.N. Jing, X.L. Yin, L.L. Li, Y.L. Wang, D.Q. Liu, Z.F. Xu, C.W. Chen, E.K. Liu, B. C. Han, CuO/TiO2 S-Scheme heterostructure for efficient photocatalytic CO2 reduction with nearly 100 % CO selectivity, Ceram. Int. 51 (2025) 8260–8268, https://doi.org/10.1016/j.ceramint.2024.12.255.
[93] N.N. Amerhaider Nuar, S.N.A. Siti Nurul, F. Li, I.D. Mat Azmi, P.C. Chiang, T.S. Y. Choong, Synthesis of controlled-release calcium peroxide nanoparticles coated with dextran for removal of doxycycline from aqueous system, Polymers 14 (2022), https://doi.org/10.3390/polym14183866.
[94] B. Wijaya, D.O.B. Apriandanu, R.M. Surya, Y. Yulizar, N.S. Sambudi, M. Khalil, A. Umar, Synthesis of novel TiO2/CeFeO3 heterojunction using Mugwort (Artemisia vulgaris) leaves extracts with enhanced photocatalytic activity under visible light irradiation, Appl. Surf. Sci. Adv. 21 (2024), https://doi.org/10.1016/j.apsadv.2024.100599.
[95] S.K. Filippov, R. Khusnutdinov, A. Murmiliuk, W. Inam, L.Y. Zakharova, H. Zhang, V.V. Khutoryanskiy, Dynamic light scattering and transmission electron microscopy in drug delivery: a roadmap for correct characterization of nanoparticles and interpretation of results, Mater. Horiz. 10 (2023) 5354–5370, https://doi.org/10.1039/d3mh00717k.
[96] N.K. Sethy, Z. Arif, P.K. Mishra, P. Kumar, Green synthesis of TiO2 nanoparticles from Syzygium cumini extract for photo-catalytic removal of lead (Pb) in explosive industrial wastewater, Green Process. Synth. 9 (2020) 171–181, https://doi.org/10.1515/gps-2020-0018.
[97] M. Scimeca, S. Bischetti, H.K. Lamsira, R. Bonfiglio, E. Bonanno, Energy dispersive X-ray (EDX) microanalysis: a powerful tool in biomedical research and diagnosis, Eur. J. Histochem. 62 (2018) 89–99, https://doi.org/10.4081/ejh.2018.2841.
[98] Microscopy Australia, Energy dispersive spectroscopy, MyScope. www.myscope.training, 2025. (Accessed 18 August 2025).
[99] B. Bai, G. Cheng, J. Chen, X. Chen, Q. Wang, Strong magnetic p-n heterojunction Fe3O4-FeWO4 for photo-fenton degradation of tetracycline hydrochloride, Catalysts 14 (2024), https://doi.org/10.3390/catal14070453.
[100] S. Dong, Y. Yang, A. Zada, S. yuan Liu, K. Qi, Performance and mechanism of photocatalytic tetracycline degradation by AgInS2/ZnS composites, J. Water Proc. Eng. 73 (2025), https://doi.org/10.1016/j.jwpe.2025.107695.
[101] W. Li, Synthesis and applications of mesoporous nanostructures, in: Encyclopedia of Nanomaterials, Elsevier, 2023, pp. 322–335, https://doi.org/10.1016/B978-0-12-822425-0.00054-3.

[102] S. Mandal, S. Ishak, M.A. Mohd Ariffin, D.E. Lee, T. Park, Effect of pore structure on the thermal stability of shape-stabilized phase change materials, J. Mater. Res. Technol. 25 (2023) 465–479, https://doi.org/10.1016/j.jmrt.2023.05.217.
[103] S. Wang, O. Salim, M. Piri, The effects of pore shape and geometry on the storage of CO2 in mesoporous media, Mater. Today Sustain. 29 (2025), https://doi.org/10.1016/j.mtsust.2025.101076.
[104] S. Devi, N. Aarushi, S. Tyagi, Porous zinc-discs as nanocatalysts for methylene blue dye treatment in water: sensing, adsorption and photocatalytic degradation, RSC Adv. 12 (2022) 34951–34961, https://doi.org/10.1039/d2ra05245h.
[105] Z.H. Al Naji, Y. Slimani, M.A. Almessiere, M.A. Gondal, A. Thakur, M. Shariq, A. Baykal, A. Ul-Hamid, Binary ZnO/Cs0.33WO3 heterojunction: a highly effective visible light photocatalyst for the degradation of rhodamine B and methylene blue dyes, Ceram. Int. 51 (2025) 34583–34598, https://doi.org/10.1016/j.ceramint.2025.05.182.
[106] H. Liu, F. Sun, X. Li, Q. Ma, G. Liu, H. Yu, W. Yu, X. Dong, Z. Su, g-C3N4/TiO2/ZnIn2S4 graphene aerogel photocatalysts with double S-scheme heterostructure for improving photocatalytic multifunctional performances, Compos. B Eng. 259 (2023), https://doi.org/10.1016/j.compositesb.2023.110746.
[107] X. Zhou, J. Liang, L. Xu, S. Wu, M. Xie, Q. Liang, J. Luo, X. Fan, X. Zhou, X. Zhou, Weakness-complementing Z-scheme black phosphorus/TiO2 heterojunction with efficient charge separation and photocatalytic overall water splitting activity, J. Colloid Interface Sci. 689 (2025), https://doi.org/10.1016/j.jcis.2025.03.029.
[108] Y. Xia, H. Liu, F. Sun, B. Yue, X. Wang, F. Guo, Y. Zhu, H. Yu, G. Liu, W. Yu, X. Dong, Magnetically separable CuFe2O4/ZnIn2S4 heterojunction photocatalyst for simultaneous removal of Cr(VI) and CIP, J. Clean. Prod. 434 (2024), https://doi.org/10.1016/j.jclepro.2023.140445.
[109] L. Xu, Y. Di Ge, X.Y. Zhou, M.Y. Xing, X.Q. Wu, Y. Wang, L. Zhang, X. Wang, Study on the sonocatalytic removal of tetracycline by an type-II heterojunction CuS/FeWO4, J. Alloys Compd. 1015 (2025), https://doi.org/10.1016/j.jallcom.2025.178826.
[110] Y. Wu, Y. Guo, Y. Gao, B. Ma, Y. Xu, S. Yang, X. Wang, W. Zhao, Y. Liu, Dual-function reusable substrates based on magnetic S-scheme ZnFe2O4-Cu2O-Au nanocomposites: efficient photocatalytic degradation and sensitive SERS detection of ciprofloxacin, Ceram. Int. (2025), https://doi.org/10.1016/j.ceramint.2025.08.130.
[111] Y. Chu, Y. Zheng, J. Xu, R. Dong, F. Zhu, K. Wang, Y. Wu, Y. He, Mechanistic insights into MnO_x -cocatalyzed piezophotocatalytic dye degradation over S-scheme MnO_x/$BiFeO_3$ heterojunctions, Inorg. Chem. Front. (2025), https://doi.org/10.1039/D5QI01226K.
[112] N. Ramesh Reddy, P. Mohan Reddy, J. Hak Jung, S. Woo Joo, Construction of various morphological ZnO-NiO S-scheme nanocomposites for photocatalytic dye degradation, Inorg. Chem. Commun. 146 (2022), https://doi.org/10.1016/j.inoche.2022.110107.
[113] P. Sharma, A. Kumar, P. Dhiman, G. Sharma, G. Tessema Mola, F.J. Stadler, Recent progress in photocatalytic applications of metal tungstates based Z-scheme and S-scheme heterojunctions, J. Ind. Eng. Chem. 132 (2024) 1–21, https://doi.org/10.1016/j.jiec.2023.11.004.
[114] M. Hosseini, M. Ghanbari, E.A. Dawi, A.M. Aljeboree, M.H.S. Alubiady, A.M. Al-Ani, M. Salavati-Niasari, Barium stannate/graphitic carbon nitride S-scheme heterojunction as an efficient photocatalyst for removal of toxic coloring agents under visible light, Surf. Interfaces 46 (2024), https://doi.org/10.1016/j.surfin.2024.104162.
[115] N.N. Amerhaider Nuar, S.N.A. Siti Nurul, T.S.Y. Choong, I.D. Mat Azmi, N. A. Abdul Romli, L.C. Abdullah, P.C. Chiang, F. Li, Synthesis of calcium peroxide nanoparticles with starch as a stabilizer for the degradation of organic dye in an aqueous solution, Polymers 15 (2023), https://doi.org/10.3390/polym15051327.